SYNTHESIS AND ELECTRICAL CONDUCTIVITY STUDY OF V^{5+}- and P^{5+}-DOPEDBISMUTH OXIDE-BASED ELECTROLYTES FOR IT-SOFC APPLICATION

Presented in Partial fulfillment of the Requirements for degree of
Master of Science

By Bhakti Naik and Diksha Karmalkar

Under the supervision of

Dr. Bholanath Pahari

Assistant Professor

Department of Physics

Goa University

20 July 2020

Acknowledgements

We would like to express our deep gratitude and respect to our guide, **Dr. Bholanath Pahari**for his keen interest and valuable guidance, strong motivation and constant encouragement during the course of work. We also thank him for his great patience, constructive criticism and useful suggestions apart from invaluable guidance. We are also grateful to **Dr. KaustubhPriolkar**, Professor and Head of department, Physics for his encouragement.

We would also like to thank, **Dr. AnupBera,** BARC, Mumbai for impedance measurements, **Mr.SantoshkumarBandaru**, PhD student of Physics Department, Goa University for his help to carry out uv-vis studies and **Mr. Mahendra Chaudhary**, research scholar atPhysics Department, Goa Universityfor his help throughout various stages of our project.

We are also thankful to all the staff members of Goa University, physics dept for their support and encouragement.

Last but not the least; we would like to thank our parentsfor their moral support.

-Bhakti Manohar Naik **-Diksha Nitin.Karmalkar**

Contents

Abstract

Solid electrolytes are essential part of solid oxide fuel cells.Currently stabilized zirconia, especially yttria-stabilized zirconia (YSZ) is extensively used as an electrolyte for SOFCs. However, its ionic conductivity decreases below 1000 °C. Hence there is a constant search for better electrolyte with lower working temperatures. Therefore, in the present study, Vanadium and phosphorus doped Bi_2O_3 compounds $Bi_{1-x}V_xO_{1.5+x}$ (x=0.087, 0.095, 0.148), $Bi_{0.852}P_{0.148}O_{1.648}$ were prepared by solid state reaction methods for its use as an electrolyte in SOFC. The samples prepared in this study were characterized using different techniques such as X-ray diffraction, UV-Vis spectroscopy and electrochemical impedance spectroscopy. Structural behavior was studied using XRD technique as function of V^{5+}, P^{5+} substitutions on Bi site. Among the four compositions, cubic phase was observed for $Bi_{0.905}V_{0.095}O_{1.595}$ and $Bi_{0.913}V_{0.087}O_{1.587}$ and monoclinic phase was observed for $Bi_{0.852}P_{0.148}O_{1.648}$ and $Bi_{0.852}V_{0.148}O_{1.648}$. Electrochemical Impedance Spectroscopy (EIS) results revealed an increase in ionic conductivity with increase in concentration of V from x=0.087 to 0.095.However, with further increase, there was decrease in conductivity. Also in case of P substitution there is a fall in conductivity. Energy band gaps of the prepared samples were determined using UV-Vis spectroscopy. It was observed that the energy band gap values of V substituted samples decreased from E=2.86 eV at x=0.087 to E=2.79 eV at x=0.095, whereas P substituted samples showed band gap value of E=3.03 eV.This range of energy band gap values indicates that the samples have negligible electronic conductivity.

CHAPTER 1

Introduction

The current energy supply systems are mainly based on the combustion of fossil fuels which can cause many environmental problems like air pollution, acid gas emissions, and the emission of greenhouse gases. At the same time supply of electricity is a basis of modern life. Thus one of the biggest challenges today is to deal both conservation of energy resources and decrease of CO_2 emission [1]. This growing concern over the depletion of fossil fuel resources and the unpredictably adverse climatic conditions has driven us to shift towards renewable energy resources. This however requires mature energy storage and conversion systems [4]. Fuel cells are one of the promising energy conversion and storage technologies that could solve some of the environmental issues, while simultaneously curbing the consumption of resources [1]. They are proposed as promising alternative for large scale generation of electricity, with minimal undesirable chemical, thermal and acoustic emissions [2].

1.1 Fuel cells

Fuel cells are electrochemical energy conversion devices that generate electricity and heat by converting the chemical energy of fuels. If we try to compare between fuel cells and batteries, we see that a battery is an energy storage device that stores its fuel internally and it can supply only a fixed amount of energy but in a fuel cell reactants are supplied externally, and thus it has no fixed capacity. Therefore, a fuel cell is capable of generating electricity as long as fuels are supplied. Another advantage of using a fuel cell is that it is fuel flexible. It can accept wide variety of fuels, including natural gas, coal gas, gaseous fuels from biomass and liquid fuels etc, although some fuel may require reprocessing and purification. Fuel cells can be classified depending on the type of the electrolyte they incorporate, but much of the interest is focused on commonly used following four types of fuel cells: **solid oxide**, **proton exchange membrane**, **molten carbonate**, and **alkaline fuel cells** [3].Electrolytes and fuels for some of the fuel cells are as tabulated below.

Table 1: Fuel cell types and their features [9]

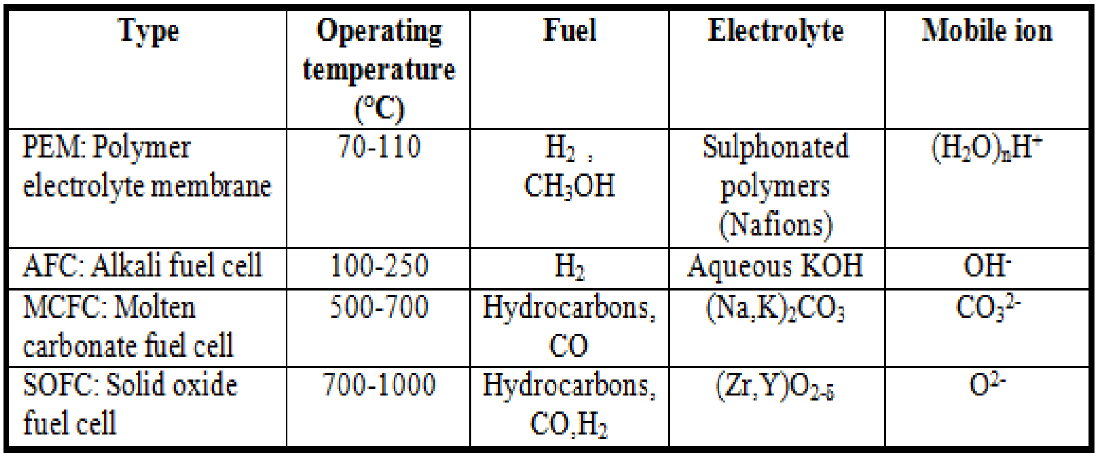

Type	Operating temperature (°C)	Fuel	Electrolyte	Mobile ion
PEM: Polymer electrolyte membrane	70-110	H_2 , CH_3OH	Sulphonated polymers (Nafions)	$(H_2O)_nH^+$
AFC: Alkali fuel cell	100-250	H_2	Aqueous KOH	OH^-
MCFC: Molten carbonate fuel cell	500-700	Hydrocarbons, CO	$(Na,K)_2CO_3$	CO_3^{2-}
SOFC: Solid oxide fuel cell	700-1000	Hydrocarbons, CO,H_2	$(Zr,Y)O_{2-\delta}$	O^{2-}

1.2 Solid-oxide Fuel Cells (SOFC)

The solid oxide fuel cell is currently attracting tremendous interest among the other fuel cells because of its huge potential to enhance energy conversion efficiency. Reliability, reducing environmental impact and fuel flexibility are its few other significant traits [4]. The efficiency of SOFC is much higher than that of conventional coal plants, which operates say at efficiency of only ~34%. But in case of SOFC when the high-quality exhaust from the electrochemical process is used; its overall efficiencies could reach 85% [3].

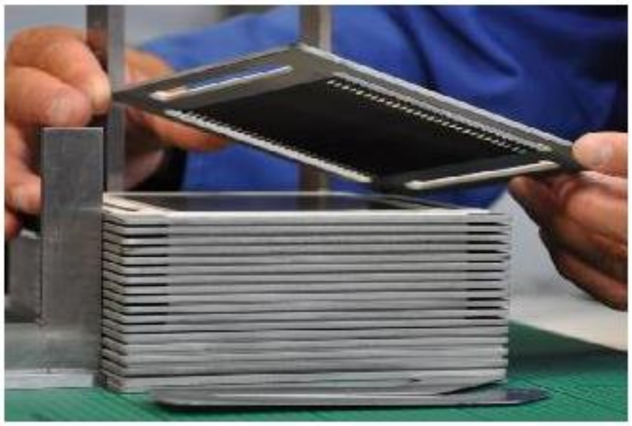

Fig. 1: SOFC fuel cell stack and single cell [17]

Principles of operation of SOFC

A SOFC is an energy conversion device that produces electricity by electrochemically combining a fuel and an oxidant across an ionic conducting electrolyte; the principle of operation can be understood from the schematic diagram shown in Fig. 2.

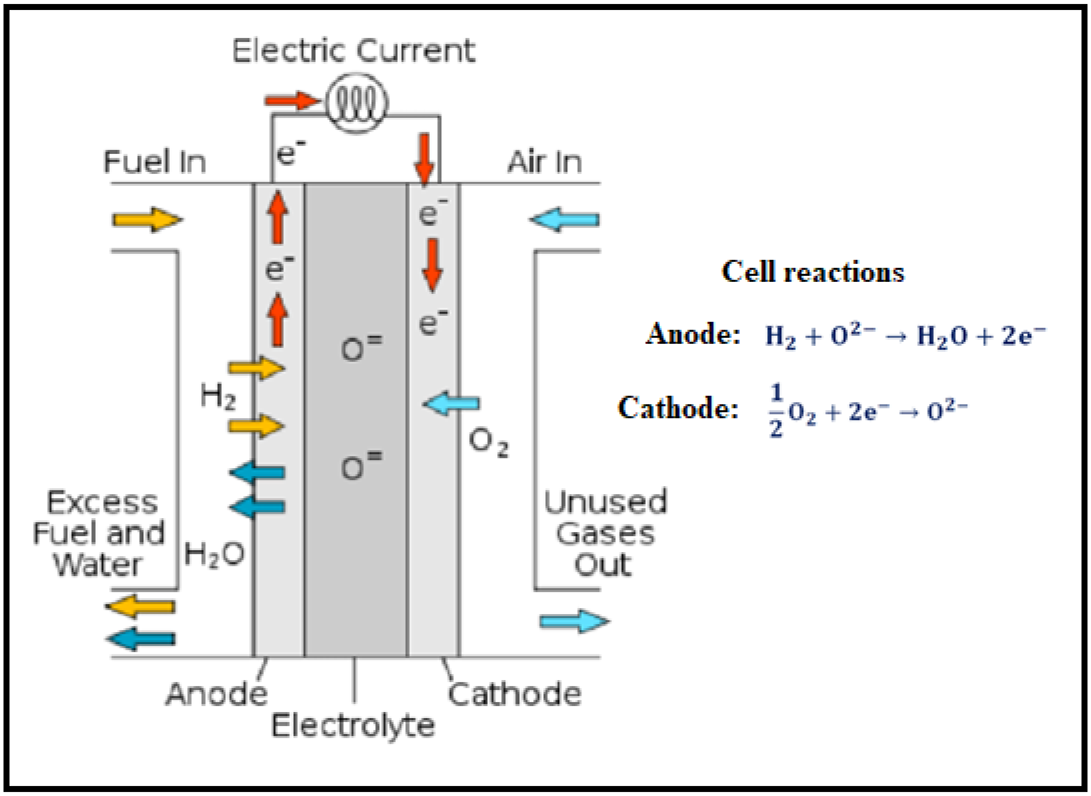

Fig. 2: Schematic diagram of SOFC and cell reactions at cathode and anode [5]

In single cell the dense electrolyte is sandwiched between two porous electrodes, the anode and the cathode. Fuel is fed to the anode; where it undergoes an oxidation reaction, and releases electrons to the external circuit. At the same time oxygen (from air) is also fed to the cathode where it accepts the electrons from the external circuit, and undergoes a reduction reaction. Amidst this, electrons flow in the external circuit from the anode to the cathode producing electricity.

In the SOFC O^{2-}, oxide ions formed by dissociation of oxygen at the cathode under electron consumption migrate through the electrolyte to the anode where they react with the oxidation products to form water. Therefore, the operation of a SOFC is largely depends on the performance of the electrolyte. The state-of-the-art SOFC typically operates between 800 and 1000 °C, because the materials generally utilized as electrolyte in the SOFCs show good O^{2-} conductivity only at high temperatures. Such high temperature conditions limit the use of SOFCs [1]. To mitigate the problem there is constant effort to search and design of better electrolyte material.

1.3 Components of SOFC

Solid oxide fuel cell essentially consists of two porous electrodes separated by a dense, oxygen ion conducting electrolyte. Electrodes in fuel cell are a place where the redox processes take place.

The fuel cell electrodes in the SOFC have the following properties:

1. High electronic conductivity.
2. Chemical and dimensional stability in environments encountered during cell operation and during fabrication of interconnection, electrolyte and fuel electrode layers.
3. Thermal expansion matches with other cell components.
4. Compatibility and minimum reactivity with the electrolyte and the interconnection with which air electrode comes into contact.
5. Compatibility and minimum reactivity with the electrolyte and the interconnection with which air electrode comes into contact.

1.3.1 Anodes (fuel electrode)

The main function of a SOFC anode is to provide electrochemically active sites for the oxidation of the fuel gas molecules and to transport electrons from the site of oxidation to connecting cell components. They thus provide pathways for the fuel to reach the reaction sites and for the reactants to diffuse away from the reaction sites.

The early designs of SOFC considered noble metals such as palladium, silver, platinum and gold and transition metals such as manganese, iron, cobalt, nickel and copper suitable materials for anode.

Anodes (fuel electrode) are high catalytic activity and redox stability, Ni was chosen as the best choice. However, the pure metal has a strong tendency towards grain growth at elevated temperatures and a significantly different thermal expansion coefficient than commonly used electrolyte materials.

Therefore, nickel is combined with a ceramic compound, such as zirconia or ceria, forming three interconnected frameworks of metal, ceramic and pores. This cermet becomes a good metallic conductor for nickel. The ceramic network not only provides structural integrity and hinders the trapped nickel particles from excessive grain growth but also provides a pathway for oxygen ions, effectively extending the triple phase boundary from the flat electrolyte interface into the anode structure. [18]

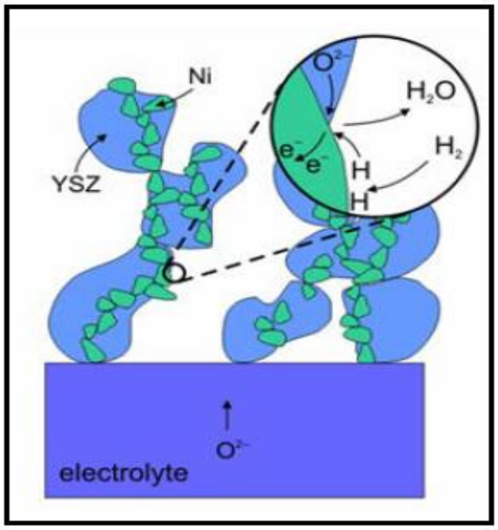

Fig. 3: Oxidation reaction on the surface of an anode made of Ni-YSZ [20].

1.3.2 Cathode (air electrode)

Cathode operates in an oxidizing environment of air or oxygen at 1000°C and participates in the oxygen reduction reaction, which determines the efficiency of the fuel cell and hence plays an important role in the fuel cell [19, 20].Also the highly oxidizing environment of cathode, eliminates the possibility to use cheap base metals [20].Therefore, the choice of cathode materials is rather limited. Although noble metals such as Pt are considered suitable, but their prohibitive costs for SOFC application at higher temperatures compels one to look for better alternatives.

Usually $La_{1-x}Sr_xMnO_{3-x/2}$ (LSM) is used for the cathode when YSZ is used as the electrolyte, because their thermal expansion coefficients match well. Also the mixed ion conductors like La_{1-}

$_{x}Sr_{x}CoO_{3-\delta}$ (LSC) based cathodes are considered. Apart from high electronic and ionic conductivity, MIECs are also feasible for use at low temperatures. This is because of its high ionic conductivity which provides a second pathway for oxygen ions and hence increases its activity. But these materials react with YSZ, thus either ceria-based electrolytes or protective layers of ceria or LSGM on YSZ electrolytes should be used. [18].

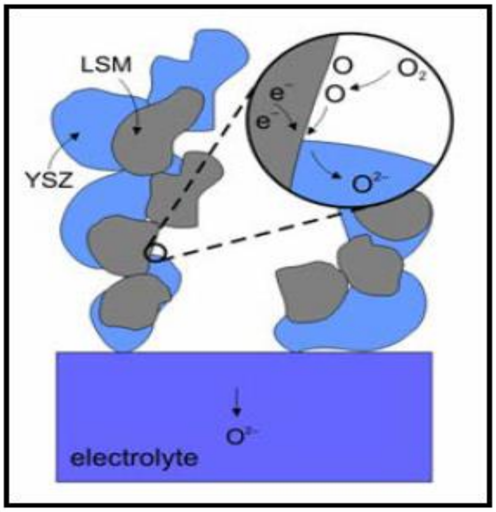

Fig. 4: Reduction reaction on the surface of a cathode made of LSM-YSZ [20].

1.3.3 Solid electrolyte

The solid electrolyte is the central component that determines the operational characteristics of the fuel cell system, namely the working temperature. Designing new electrolytes includes manipulation of ionic defects concentration and mobility [6].The general criteria for the quality of a solid electrolyte material to be used in a SOFC are:

- High ionic conductivity of the range, $\sigma_0 > 10^{-2}$ S/cm at the cell operating temperature
- Negligible electronic conductivity
- Compatibility with the cell components
- Low reactivity
- Compatibility of thermal-expansion coefficients between electrolytes, electrodes.
- Relatively low costs of material and fabrication.

SOFCs are unique with respect to other types of fuel cells for using a ceramic oxide as solid electrolyte.Under operation, the SOFC can use either an oxygen ion-conducting electrolyte or a proton conducting electrolyte, and however most of the current research efforts have been focusing on the SOFC with the oxygen ion-conducting electrolyte [1, 6].

1.4 Oxide ion conductor

They are group of advance ceramic materials, and are most reasonably accepted as the electrolyte in SOFCs. By using oxide ion conductors as the electrolyte, hydrocarbon can be directly used as fuel, and thus, it is possible to use various fuels, which is one of the advantages of SOFCs using oxide ion conductors [7]

In oxygen ion conductors, current flow occurs by the movement of oxide ions through the vacancies. This movement is a result of thermally-activated hopping of the oxygen ions, moving from crystal lattice site to crystal vacant site, with a superimposed drift in the direction of the electric field. The ionic conductivity is consequently strongly temperature dependent, and at high temperatures its value can approach close to 1 S/cm. This type of conduction requires the crystal to contain unoccupied sites equivalent to those occupied by the lattice oxygen ions. Secondly, the energy involved in the process of migration from one site to the unoccupied equivalent site must be small [9]. Therefore, in general the conductivity of any electrolyte can be given as a combined sum of ionic and electronic contributions,

$$\sigma = \sigma_i + \sigma_e = n_i \mu_i (z_i e) + n_e \mu_e e \cdots\cdots (1)$$

If the electronic conductivity is negligible and there is only a single mobile ionic species, above equation further reduces to

$$\sigma = \sigma_i = n_i \mu_i (z_i e). \cdots\cdots (2)$$

Where, n_i, μ_i and $(z_i e)$ are respectively the concentration, mobility and charge of the mobile species. Since ions move via defects in the crystal lattice and each type of defect has energies of formation and motion associated with it, we can define this energy as the activation energy E_a and the ionic conductivity can then be given as

$$\sigma = \frac{\sigma_0}{T} e^{-\frac{E_a}{k_B T}} \cdots\cdots (3),$$

Where the pre-exponential term may be expressed as,

$$\sigma_0 = \frac{1}{3k_B} z^2 e^2 n a^2 \omega_0 \cdots\cdots (4).$$

In Eqn. (4) a is the jump distance and ω_0 is the attempt frequency [8].

Oxide ion conductors are also important and technologically exploitable materials used in several types of devices for energy-related and environmental applications. These include oxygen sensors and pumps, dense membranes for oxygen permeation [10].

Well-known oxide ion conductors having good O^{2-} ion conduction property are shown in the plot below.

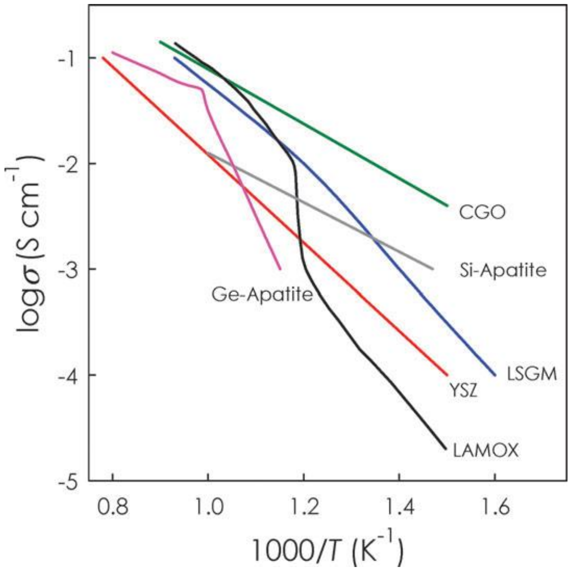

Fig. 5: Total conductivities of several well-known oxide-ion conductors as a function of inverse temperature [5].

Table 2: Conductivities of several well-known oxide ion conductors [5]

Electrolyte	Temperature (°C)	Conductivity (Scm^{-1})
YSZ $(ZrO_2)_{0.92}(Y_2O_3)_{0.08}$	500	$9x10^{-4}$
CGO $Ce_{0.8}Gd_{0.2}O_{1.9}$	500	$2x10^{-2}$
LSGM $La_{0.9}Sr_{0.1}Ga_{0.8}Mg_{0.2}O_{2.85}$	500	$7x10^{-3}$
LAMOX $La_2Mo_2O_9$	500	$5x10^{-4}$
Si-apatite $La_{10}(SiO_4)_6O_3$	500	$5x10^{-3}$
Ge-apatite $La_{10}(GeO_4)_6O_3$	727	$5x10^{-2}$

As can be seen in the plot, most of the oxide ion conductors have high ion conductivity at high temperature (<800 °C). Thus the obstacle in the commercialization of SOFCs is their high operating temperature. It is reasonable to consider that the fuel cell operating temperature mostly depends on the choice of the electrolyte material. Thus the choice of the electrolyte material, conductivity, stability and the availability of suitable techniques for fabrication of thin films become critical issues in consideration of the lower temperature operation. Lowering the operating temperature is advantageous since it can help reduce the cost for operation and materials. Also the cell degradation problems, such as inter-diffusion between cell components, can be mitigated [4].

Currently stabilized zirconia, especially yttria-stabilized zirconia (YSZ) is extensively used as an electrolyte for SOFCs.YSZ is one of the best oxide ion conductors and its high-temperature polymorph has fluorite crystal structure and may be stabilized to room temperature by formation of solid solutions with CaO, Y_2O_3, etc. Stabilized zirconia exhibits high O^{2-}ion conductivity at high temperatures because of the mechanism of solid solution formation which involves the creation of vacant O^{2-}sites in order to preserve electro neutrality [11]. Other O^{2-}ion conductors are Bi_2O_3andZrObased compound. However, compared to Bi_2O_3, solid electrolytes based on ZrO, have relatively low oxide ion conductivity at temperatures below 800 K and require very high sintering temperatures (often higher than 2000 K) [12].

1.5 Pure bismuth oxide (Bi_2O_3)

Pure bismuth oxide has two thermodynamically stable polymorphs. One is α-Bi_2O_3, which is stable below 730° C and has monoclinic structure. The other is δ-Bi_2O_3 which is stable above 730°C up to its melting point at 825° C.δ-Bi_2O_3phase crystallises in fluorite-type structure. As can be seen in panel (a) of the Figure 6 the α-phase of Bi_2O_3 transforms to the δ-phase, when it is heated above 729°C.This transformed phase is retained until the melting point of Bi_2O_3 is reached (824 °C). In panel (b) of the Figure 6 it is shown that on cooling, the δ-phase transforms to either of its two metastable phases i.e.

i. β-phase at 650 °C, which then transforms to α-phase at 303 °C.
ii. γ-phase at 639 °C, which may persist to room temperature if the cooling rate is slow, otherwise it transforms to α-phase at 500 °C [21]

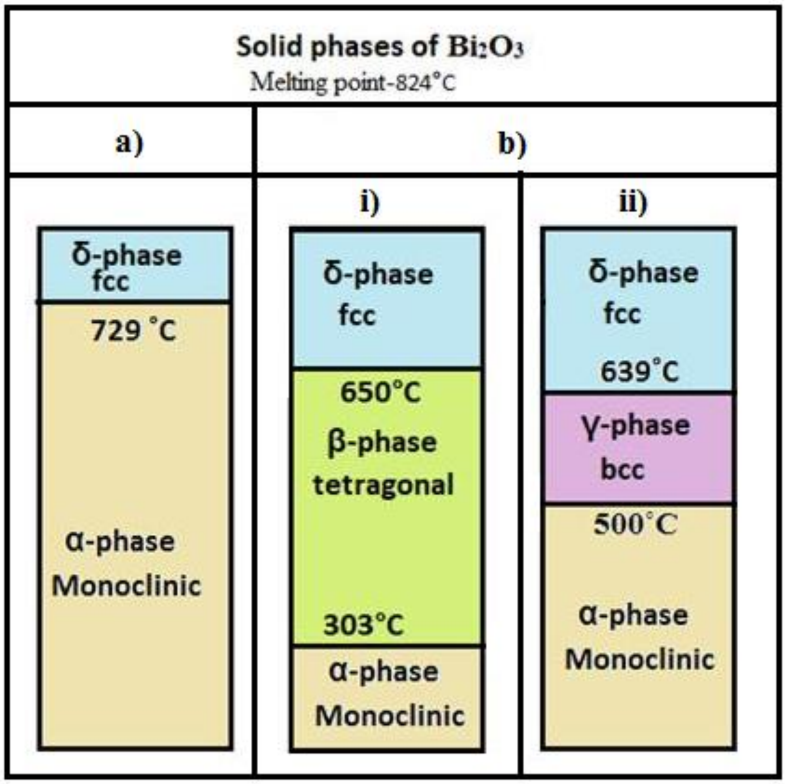

Fig.6: Existing domains of four polymorphs of Bi_2O_3 phases as a function of temperature [15]

The value of O^{2-} ion conductivity measured in different phases of Bi_2O_3 is tabulated below.

Table 3: Conductivity of various phases of Bi_2O_3 [13]

Phase	Conductivity at 600 °C (Scm^{-1})	Conductivity at 650 °C (Scm^{-1})
α-Bi_2O_3	$\sim 10^{-4}$	3×10^{-4}
β-Bi_2O_3	$\sim 10^{-4}$	2×10^{-3}
γ-Bi_2O_3	$\sim 3\times10^{-3}$	5×10^{-3}
δ-Bi_2O_3	-	1

The fluorite-based structure of δ-Bi_2O_3 is shown in the Fig. 7.Because Bi is trivalent, each non primitive unit cell contains an average of six oxygen atoms, rather than eight as in the fluorite structure itself. That is, the structure can be considered as a fluorite structure with an intrinsic deficiency of two oxygen atoms per unit cell. Thus δ-Bi_2O_3 has oxygen vacancy density of a highly doped fluorite structure, however, without the dopants themselves.

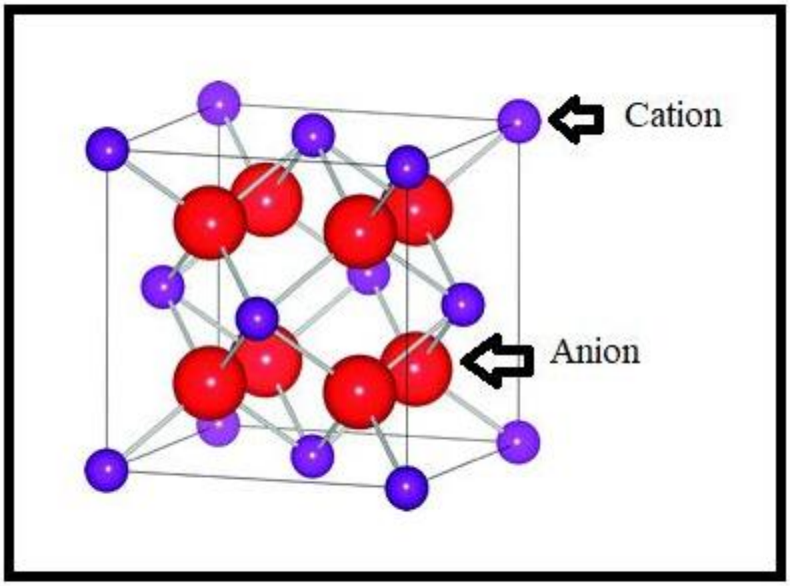

Fig 7: Fluorite structure of a typical oxide ion conductor [16]

This high-temperature cubic fluorite-type bismuth oxide, δ-Bi_2O_3, with intrinsic oxygen vacancies, shows the highest oxide ion conductivity measured in any material (~1 S/cm at 750 °C). It is understood that the high conductivity of δ-Bi_2O_3 can be attributed to high polarizability of theBi^{3+} cations, with its $6s^2$ lone pair of electrons which favours oxide ion mobility as well as weak Bi-O bond [12].

1.6 Motivation

The transition from the high temperature δ-Bi_2O_3 to the intermediate β-Bi_2O_3 is accompanied by a large volume change and as a result there is deterioration of the mechanical properties of the materials. It is therefore necessary to stabilise δ-Bi_2O_3 to room temperature to avoid problems associated with phase transitions, before it is suitable for practical use as solid electrolyte.δ-Bi_2O_3 can be stabilized to the lower temperature by dopants which include rare-earth elements or many oxide impurities. Also conductivity can be further enhanced by doping [14]. Herein, we have attempted to examine the possibility of stabilization of the cubic fluorite-type structure at room temperature in Bi_2O_3 by V^{5+} and P^{5+} doping and examine ionic conductivity.

CHAPTER 2

Methodology and characterization

2.1 Sample Preparation

Bismuth Vanadate, $Bi_{1-x}V_xO_{1.5+x}$ with vanadium concentration of x=0.087, 0.095 and 0.148 and Bismuth Phosphate, $Bi_{0.852}P_{0.148}O_{1.648}$ were prepared using Bi_2O_3 (99.9%, Sigma-Aldrich), V_2O_5 (99.99%, Sigma-Aldrich) and $NH_4H_2PO_4$ (≥98%, Sigma-Aldrich) via solid state reactions.

$Bi_2O_3 + V_2O_5 \rightarrow Bi_{(1-x)}V_xO_{(1.5+x)}$, For x=0.087, 0.095, 0.148…… Reaction (1)

$Bi_2O_3 + NH_4H_2PO_4 \rightarrow Bi_{0.852}P_{0.148}O_{1.648} + NH_3 + H_2O$……. Reaction (2)

After balancing above reactions, the amount of reagents i.e. Bi_2O_3, V_2O_5 and $NH_4H_2PO_4$ required to synthesize 2 gm of $Bi_{1-x}V_xO_{1.5+x}$for x=0.087, 0.095, 0.148 and $Bi_{0.852}P_{0.148}O_{1.648}$ were calculated.

Table.4: Sample and the amount of reagent in g

Sample	Reagents	Required amount	Taken amount
$Bi_{0.913}V_{0.087}O_{1.587}$	Bi_2O_3	1.9283 gm	1.9329 gm
	V_2O_5	0.0717 gm	0.0726 gm
$Bi_{0.905}V_{0.095}O_{1.595}$	Bi_2O_3	1.9212 gm	1.9219 gm
	V_2O_5	0.0787 gm	0.0789 gm
$Bi_{0.852}V_{0.148}O_{1.648}$	Bi_2O_3	1.873 gm	1.8771 gm
	V_2O_5	0.127 gm	0.1292 gm
$Bi_{0.852}P_{0.148}O_{1.648}$	Bi_2O_3	1.8995 gm	1.9003 gm
	V_2O_5	0.1629 gm	0.1634 gm

Stoichometric mixtures were weighed using an electronic 4-digit balance. They were thoroughly mixed in isopropanol for 2 h, using mortar and pestle and dried by evaporation in air. This mixture was then heated at 700,750,800 ºC and finally at 825 ºC for the Vanadates and 850 ºC for the Phosphate, for 12h at each temperature in silica crucible and slowly cooled until room temperature was reached (using heating and cooling rates of 5°C/min). Intermediate regrinding without isopropanol was carried out at ~12 hours intervals in order to increase the contact area and to bring fresh surfaces into contact. The calcination process was carried out in a pit furnace. The product thus obtained after heating was reground till a fine powder was obtained. For pellets preparation, sufficient amount of powder was placed in a steel die measuring 10 mm in diameter. A pressure of 1–2.5 tons was applied and held for ~30 seconds. The pellet was then sintered at its synthesis temperature, which ranged from 850 C overnight in order to increase the mechanical strength of the pellets and to reduce the intergranular resistance.

2.2Characterization of materials

2.2.1X-Ray Diffraction

X-ray diffraction is a non-destructive analytical technique which reveals information about the crystallographic structure, chemical composition, and physical properties of materials. This technique is based on observing the scattered intensity of an X-ray beam hitting a sample as a function of incident and scattered angle. It is therefore an important experimental technique used to uniquely identify the crystalline phases of the materials and to measure their structural parameters such as lattice constants, grain size, and phase composition [22].

Principle:

Max von Laue discovered that crystalline substances act as three-dimensional diffraction gratings for X-ray wavelengths similar to the spacing of planes in a crystal lattice. That means X-rays can be diffracted from materials which, by definition are crystalline and have regularly repeated atomic structures. Therefore, when certain geometric requirements are met, X-rays scattered from a crystalline solid can constructively interfere, producing a diffracted beam. This geometric condition corresponds to Bragg’s law [22].

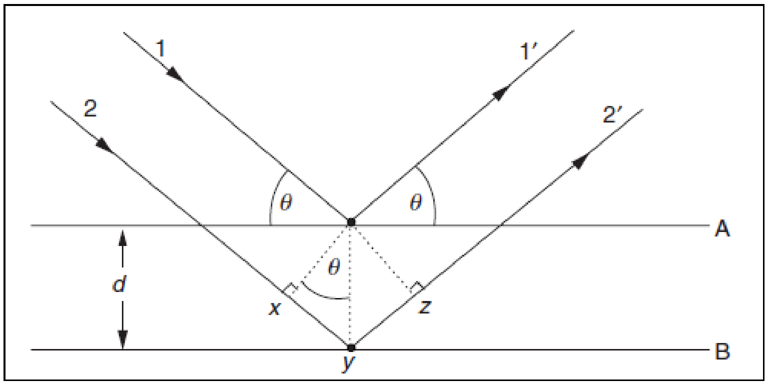

Fig.8: Derivation of Bragg's law [23]

In Bragg's approach to diffraction, crystals are considered to be built in the form of layers or planes and each plane acts as a semi-transparent mirror. Two X-ray beams, 1 and 2 are reflected from adjacent planes, A and B, within the crystal. As can be seen from Fig.1, beam 22' has to travel an extra distance *xyz* compared with beam 11'; and for 1' and 2' to be in-phase, the distance *xyz* must equal a whole number of wavelengths [23].

The relation between perpendicular d-spacing, Bragg angle (*θ)* and the distance *xy* can be given as

$$xy = yz = d \sin \theta$$

Hence,

$$xyz = 2d \sin \theta$$

However,

$$xyz = n\lambda$$

And therefore,

$$n\lambda = 2d \sin \theta \ldots\ldots (1)$$

Equation (1) is Bragg's law

Therefore, when Bragg's law is satisfied, the reflected beams are in-phase and interfere constructively, however incase of angles other than the Bragg angle, reflected beams are out-of-phase and destructive interference or cancellation occurs. For a given set of planes, several solutions of Bragg's law are usually possible, for *n* = 1, 2, 3, etc. However, it is customary to set *n=1* and for situations where, say, *n* = 2, the *d*-spacing is instead halved by doubling the number of planes in the set; hence *n* is kept equal to 1[23].

Conversion of the diffraction peaks to d-spacing allows identification of the material because each material has a set of unique d-spacing. Thus, the typical characteristic peaks provided by diffraction pattern is unique 'fingerprint' of the minerals present in the sample. Interpretation can be then achieved by comparison d-spacing with standard reference patterns [22].

Working:

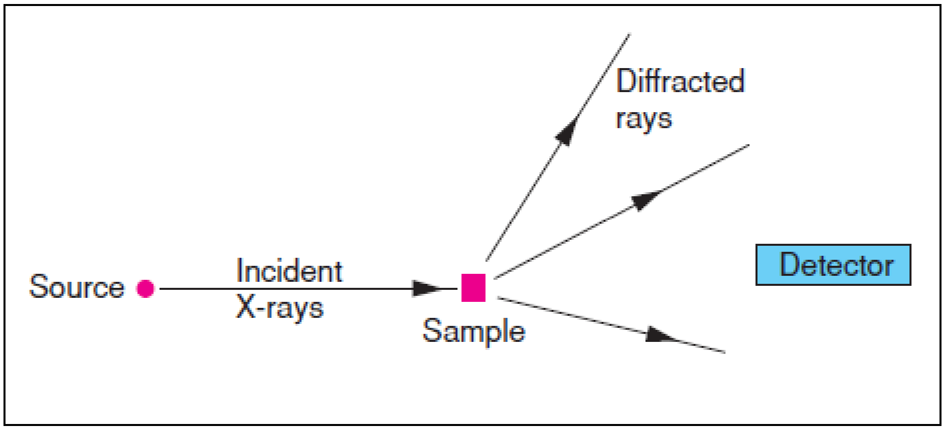

Fig.9: The X-ray diffraction experiment [23]

X-ray diffractometers consist of three basic elements:

a) Radiation-monochromatic or of variable, λ
b) Sample - single crystal, powder or a solid piece.
c) X-ray detector- radiation counter or photographic film.

In a cathode ray tube, filament is heated to emit electrons and these electrons are then accelerated towards a target by applying a voltage (≥10 kV), thus producing X-ray. However, when electrons have sufficient energy to dislodge inner shell electrons of the target material, characteristic X-ray spectra are produced. These spectra consist of several components, the most common being K_α and K_β. But for most diffraction experiments, a monochromatic beam of X-rays is desired and not a continuous spectrum and hence it is necessary to filter out all other wavelengths. These X-rays are then collimated and directed onto the sample. As the sample and detector are rotated, the intensity of the reflected X-rays is recorded. When the geometry of the incident X-rays impinging the sample satisfies Bragg's law, constructive interference occurs and a peak in intensity appears. A detector records and processes this X-ray signal and converts the signal to a count rate, which is then transferred to a device such as a printer or computer monitor [22].

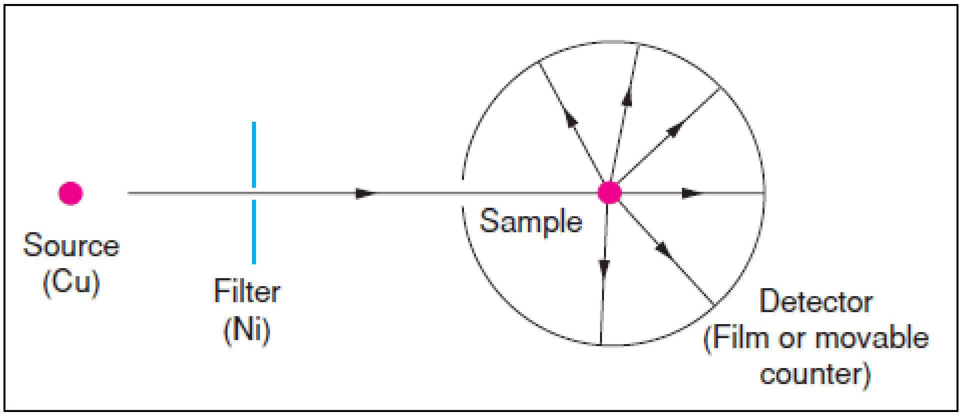

Fig.10: The powder method [23]

Copper is the most common target material with CuK_α radiation, λ=1.5418Å and Ni foil is a very effective filter for copper target.

In finely powdered sample, crystals are randomly arranged in every possible orientation and various lattice planes are also present in every possible orientation. Therefore, for each set of planes, at least some crystals must be oriented at the Bragg angle, θ, to the incident beam and thus diffraction occurs for these crystals and planes. The diffracted beams may be detected either by surrounding the sample with a strip of photographic film or by using a movable detector [25].

2.2.2 UV –Visible spectroscopy

When a beam of electromagnetic radiation interacts with a material, it can be absorbed, transmitted, scattered or reflected. UV-Visible spectroscopy refers to absorption /reflectance spectroscopy in the ultraviolet-visible spectral region. It is therefore used to measure the intensity of radiation absorbed by the sample in the wavelength range from near-ultraviolet through visible to near infra-red region and is scanned normally from 200 to 800 nm [25].

UV-Visible spectroscopy, as a technique of characterization, deals with the study of electronic transitions between orbitals or bands of atoms, ions or molecules in the gaseous, liquid and solid phase [26].Thus it can be used to find out the nature of transitions of carriers and band gap of a material by investigating measurement of the absorption edge of the material [27].

Principle

UV spectrophotometer principle follows the Beer-Lambert Law which states that transmittance i.e. the intensity of transmitted light (I_T) over the incident intensity (I_0), is dependent on the path length of the light through the sample (l), the absorption cross section (σ) of the sample's transition, and the difference in the population of the initial state (N_1) and final state (N_2),

$$T = \frac{I_T}{I_0} = e^{-\sigma(N_1 - N_2)l} \ldots\ldots (1)$$

This is often written in a form referred to as Beer's Law, equation (2)

$$\mathrm{A} = \varepsilon c l = -\log_{10}\left(\frac{I_T}{I_0}\right)$$

Or,

$$I_T = I_0(10)^{-\varepsilon c l} \ldots\ldots. (2)$$

Where, A is the absorbance, ε is the molar absorptivity coefficient of the material, *c* is the concentration of the absorbing species, and *l* is the path length of the light through the sample

[24].

The absorbance *A* can be normalized to the path length l of the light through the material (e.g. the thickness) producing the absorption coefficient α,

$$\alpha(cm^{-1}) = \frac{\ln(10) \times A}{l(cm)}$$

Or,

$$\alpha(cm^{-1}) = \frac{2.303 \times A}{l(cm)}$$

If a beam of photons with hν >Eg falls on a material, there will be some predictable amount of absorption determined by the properties of the material.

The intensity of light transmitted through the sample of thickness, l is given by

$$I_T = I_0 e^{-\alpha l}$$

Near the absorption edge, the absorption coefficient is then expressed as

$$\alpha \sim (E_g - h\nu)^{\gamma}$$

Where, hν is the photon energy, E_g is the optical gap, γ is a constant which is equal to 1/2 and 3/2 for allowed direct transition and forbidden direct transition whereas it is equal to 2 for indirect transition. The shape of the UV-vis absorption spectrum can distinguish between these transitions [24, 28].

In materials with a large exciton binding energy, absorbed photon will have barely enough energy to create an exciton, but not enough energy to separate the electron and hole. Therefore, in such a case, there is a distinction between optical band gap and electrical band gap (transport gap). The optical band gap is the threshold for photons to be absorbed, whereas the transport gap is the threshold for creating an electron–hole pair that is not bound together. The optical band gap is at lower energy than the transport gap and the difference between the two energy gaps is the binding energy of the exciton. [29].

Working

A spectrophotometer generally consists of four components:

1. Light source which covers the UV-VIS spectrum of interest. In general, a lamp containing a gas such as xenon, or a combination of two different lamps such as tungsten/deuterium is used.
2. An appropriate sample holder is needed to hold the sample.
3. A dispersion element is needed to distribute the light into separate wavelengths. It can be either a quartz prism or a diffraction grating.
4. Finally, the transmitted light intensity is recorded by a suitable detector such as photomultiplier, a multichannel array (e.g. a photodiode array, or PDA), or a charge-coupled device (CCD).

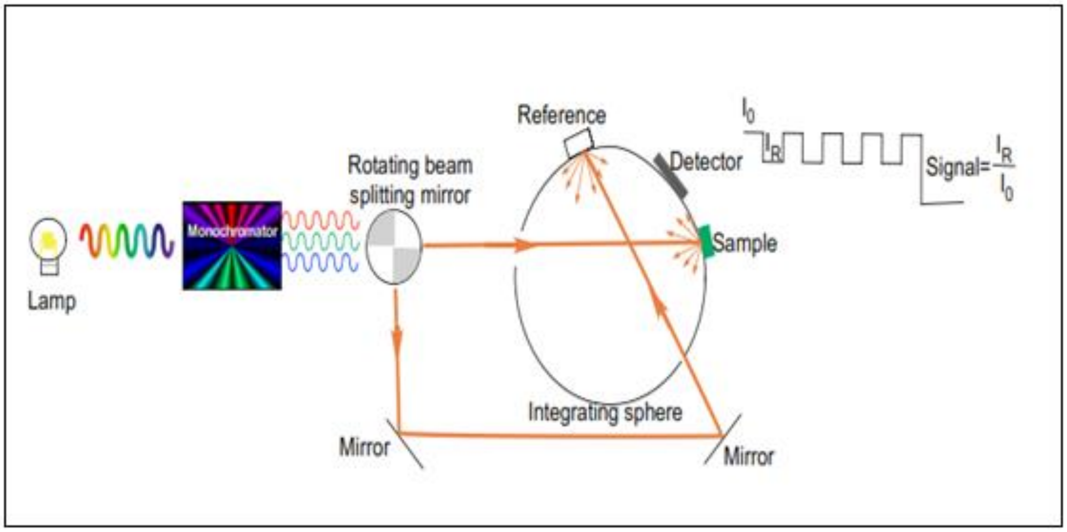

Fig.11: Optical system of a dual-beam reflectance spectrophotometer [24]

The two most commonly used UV-vis configurations are transmission and diffuse reflectance. In general, transmission mode is used for transparent samples. Often these materials are single crystals or thin films supported on transparent glass substrates. Opaque or translucent samples, such as materials supported on metallic substrates or solids made up on small particles or multiple small crystals, cannot be used since they strongly scatter light and therefore in transmission mode the spectrometer would indicate complete absorption across all wavelengths of light. As such, opaque samples must utilize a diffuse reflectance configuration. Both techniques follow the general experimental format:

- Turn on lamp source and allow at least 15 minutes for lamp to warm up
- Place reference sample into the light path. All the absorption spectra and transmission spectra were recorded keeping air as the reference and reflection spectra was taken by keeping Ba_2SO_4 as reference.
- Collect a baseline of the reference sample
- Place working sample into the light path
- Collect transmission/reflection spectrum of working sample
- Calculate the absorption coefficient and convert wavelength from nm to eV
- Fit the spectrum to estimate the band gap and assess whether it is direct or indirect and whether it is forbidden or allowed [24].

2.2.3 Electrochemical impedance technique

Electroceramics are advanced materials made up of constituent components which have different frequency dependences [31]. Generally, the dielectric properties in such materials arise due to inter-grain, intra-grain and electrode processes and it is important to separate these properties in order to unravel the complexities of such material and to have a control over properties [31, 32].This can be achieved using electrochemical impedance technique. Thus EIS is a highly sensitive characterization technique used to establish the electrical response of chemical systems in nondestructive manner [30].

In general ceramic placed between the electrodes can be expressed by Brickwood model which represents a ceramics composed of cubic grains of dimension l_1 and separated by grain boundaries of thickness l_2.

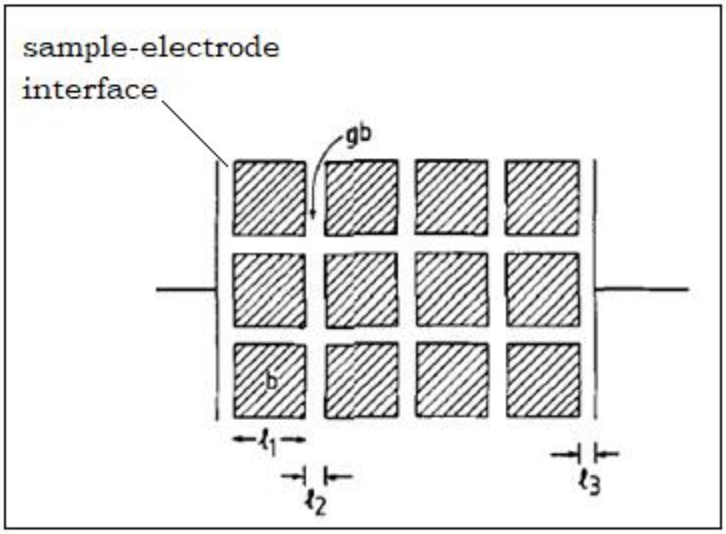

Fig.12: Brickwork model of grain and grain boundary regions in a ceramic placed between metal electrodes [31].

From the above figure, the relation $\frac{C_{gb}}{C_b} = \frac{l1}{l2}$ can be derived. [31]

Principle:

Principle of EIS is based on Faraday's Law to characterize a chemical process in terms of electrical measurements. During Impedance measurement an AC voltage is applied to a sample at different frequencies and the current is measured. The value of measured current will be determined by the mechanisms of reaction taking place within the sample. The reaction mainly involves the formation of new chemical species as result of the movement of ions through the electrolyte. Thus the flow of electric current is a result of ionic movements caused by the applied potential difference [33],

The applied ac is of form given by eq (1)

$$E(t) = E_0 \sin(\omega t) \ldots\ldots (1)$$

In order to circumvent nonlinear response of electrochemical systems EIS technique measures impedance using a small excitation signal. This perturbative ac signal ensures pseudo-linear response which means the current response to a sinusoidal potential will be a sinusoid at the same frequency but shifted in phase as can be seen in the eq (2) [32,33]

$$I(t) = I_0 \sin(\omega t + \theta) \ldots\ldots. (2)$$

The impedance can therefore be expressed as

$$Z = \frac{E(t)}{I(t)} = \frac{E_0}{I_0} \frac{\sin(\omega t)}{\sin(\omega t+\theta)} = |Z| \frac{\sin(\omega t)}{\sin(\omega t+\theta)} \ldots\ldots.. (3)$$

Thus the impedance has a magnitude $|Z|$ and phase θ and the two components of vector Z can be written in the form as given below:-

$$|Z'| = |Z| \cos \theta$$

$$|Z''| = |Z| \sin \theta$$

When ac sinusoidal voltage is applied across a pure resistance of magnitude *R*, the magnitude of impedance is *Z* = *R* and the phase θ = 0 for all frequencies. However, in case of a pure capacitance, the impedance is given as *Z* = 1/ω*C* and phase θ=90°. Thus the impedance is frequency dependent and as frequency increases impedance decreases [33]. EIS can therefore be used in analysis ceramic samples where different regions are characterized by a resistance and a capacitance, usually placed in parallel and the characteristic time constant of each ‘parallel *RC* element’ is given by[31] eq(4)

$$\tau = RC$$

Analysis of the impedance data is carried out using complex plane method. The complex series impedance$Z = Z^{'} - jZ^{"}$, is represented by a plot of real component $Z^{'}$ vs. imaginary component $Z^{"}$.This plot is commonly called as Cole-Cole plot or complex plane plot.

The total impedance Z of the circuit containing one parallel RC component is given by,

$$Z = \frac{R}{1+j\omega CR} = Z' - jZ^{"} \text{........ (5)}$$

Therefore,

$$Z' = \frac{R}{1+(\omega cR)^2} \text{ .... (6)}$$

And,

$$Z^{"} = \frac{\omega CR^2}{1+(\omega cR)^2} \text{...... (7)}$$

Eliminating ω , we get

$$(Z' - {}^{R}/_{2})^2 + (Z^{"} - 0)^2 = (R/2)^2 \text{ .... (8)}$$

Eq (8) represent the equation of a circle with center coordinate (R/2, 0) and radius equal to R/2. When we plot, $Z^{"}$vs. of the co-ordinate at the top of the semi-circular arc, at a particular frequency ω_o is (R/2, R/2). Thus, by substitution of Z’ = R/2 and Z” = R/2 in Equations (6) and (7), the relation $\omega_o RC = 1$ is obtained,

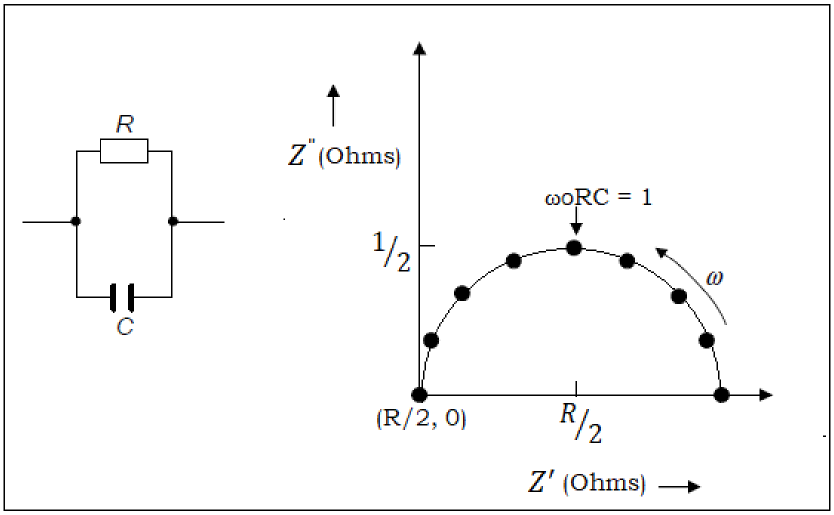

Fig.13: Complex plane impedance Spectrum-Parallel resistance, capacitance [33].

Therefore in frequency domain, different RC elements are separable due to the relation, $\omega_o RC = 1$ where ω_0 is the frequency of maximum loss in impedance spectrum.

In order to account for grain and grain boundary effects, equivalent circuit will now consist of a series collection of two sub-circuits (consisting of a resistor and capacitor connected in parallel).The complex impedance for the equivalent circuit is given by:

$$Z = \frac{1}{\frac{1}{R_g} + j\omega C_g} + \frac{1}{\frac{1}{R_{gb}} + j\omega C_{gb}} = Z' - jZ^{"} \ldots\ldots \ (9)$$

Where R_g and C_g are bulk resistance and capacitance respectively and R_{gb} and C_{gb} are grain boundary resistance and capacitance respectively.

Therefore,

$$Z' = \frac{R_g}{1 + (\omega C_g R_g)^2} + \frac{R_{gb}}{1 + (\omega C_{gb} R_{gb})^2}$$

And

$$Z^{"} = \frac{\omega C_g {R_g}^2}{1 + (\omega C_g R_g)^2} + \frac{\omega C_{gb} {R_{gb}}^2}{1 + (\omega C_{gb} R_{gb})^2}$$

Based on the above equations, the response peaks of the grains and grain boundaries are represented by 1/ (2πRgCg) and 1/ (2πRgbCgb) respectively, and the peak values are proportional to the associated resistance.

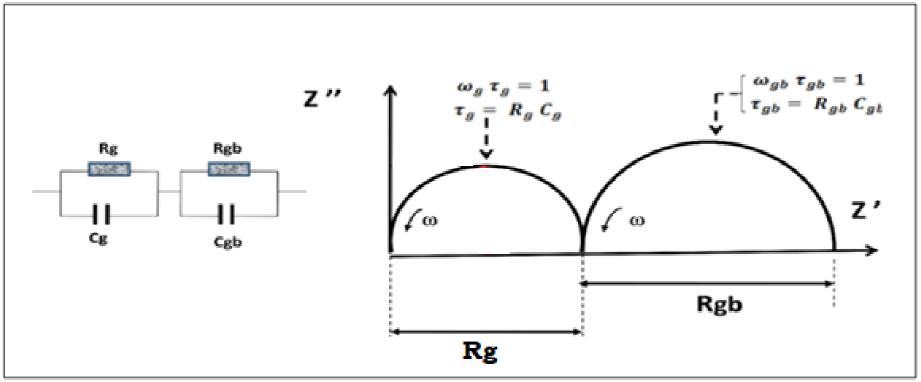

Fig.14: Nyquist plot for equivalent circuit containing two parallel RC elements in series [35]

Working

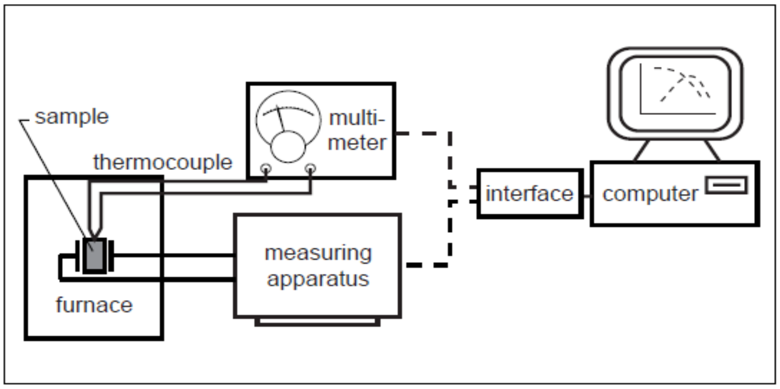

Fig.15: Experimental setup of EIS system set up [34].

In this technique, AC impedance measurements are made over a wide range of frequencies typically from 10^{-2} to 10^{7} Hz and different contributions to the overall response arising from bulk (grains), grain boundaries, and electrodes can be determined [31].

The measuring apparatus is directly connected to the sample and generates the electrical data. Measurements at different temperatures are obtained by placing the sample into a temperature-controllable furnace. A thermocouple is placed near the sample to verify the temperature, read either in terms of induced voltage (millivolts) or temperature. For automated data acquisition, the measuring system can be directly coupled to a computer through the appropriate interface. In case of frequency-domain, the sample's electrical data are recorded by means of frequency response analyzers, impedance analyzers, or high-precision inductance–capacitance–resistance meters. Once this data is obtained, it can be presented in a form of complex diagrams. Thereafter the parameters of an equivalent circuit are fitted to reproduce the measured impedance spectra. These circuit parameters are then associated with the physical and chemical processes occurring in the material [35]

CHAPTER 3

Results and Discussions

3.1 Phase identification using powder x-ray diffraction method

Polycrystalline Bi_2O_3-M_2O_5, M = P, V systems were prepared by solid state reactions. The phase purity of all the materials were determined by powder X-ray diffraction (XRD).The X-ray powder diffraction data was collected for all samples at room temperature in the range of 10°≤2θ≤80° at the scan speed of 2°/min using monochromatic Cu Kα radiation having 1.54 Å wavelength.

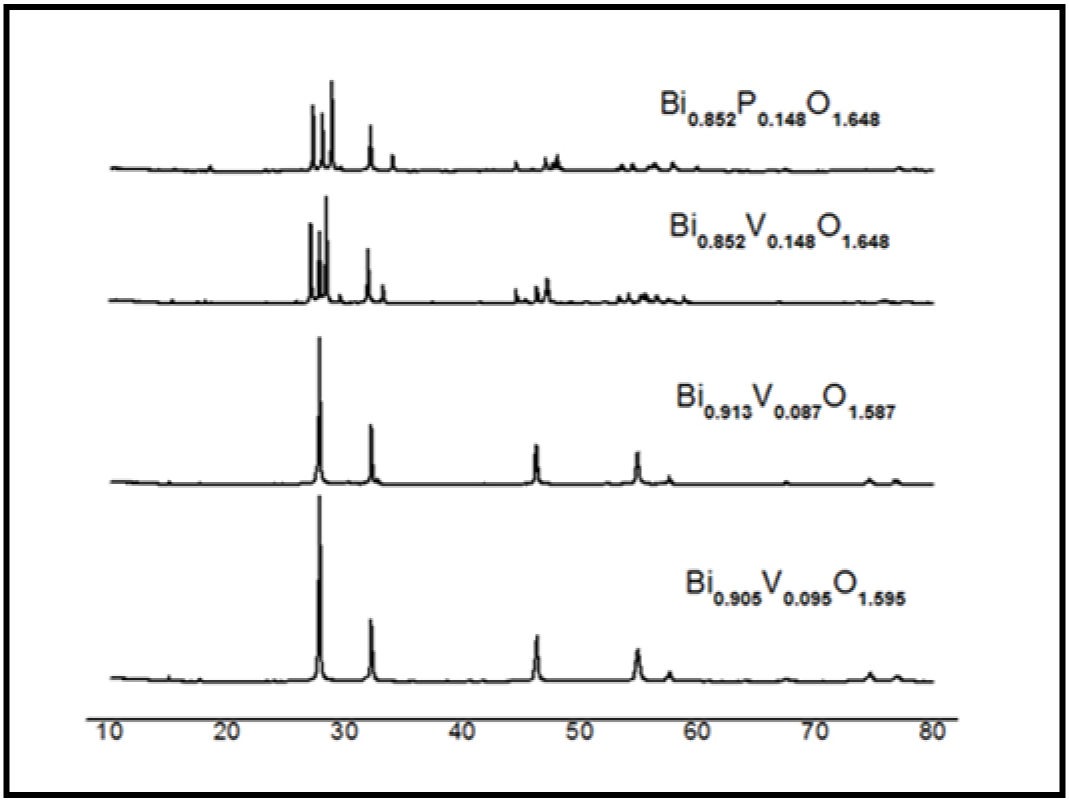

Fig.16:X-ray diffraction patterns of Bi_2O_3doped samples are shown in Figure

Fig. 16 shows the XRD stack plot of the prepared samples. Among the four compositions, cubic phase was observed for $Bi_{0.905}V_{0.095}O_{1.595}$and $Bi_{0.913}V_{0.087}O_{1.587}$and monoclinic phase was observed for $Bi_{0.852}P_{0.148}O_{1.648}$ and $Bi_{0.852}V_{0.148}O_{1.648}$.The XRD data was analyzed using CELREF software, which was also used to refine cell parameters from diffraction data by iterative least squares refinement of initial cell parameters. Results of the XRD data analysis by CELREF are as shown below

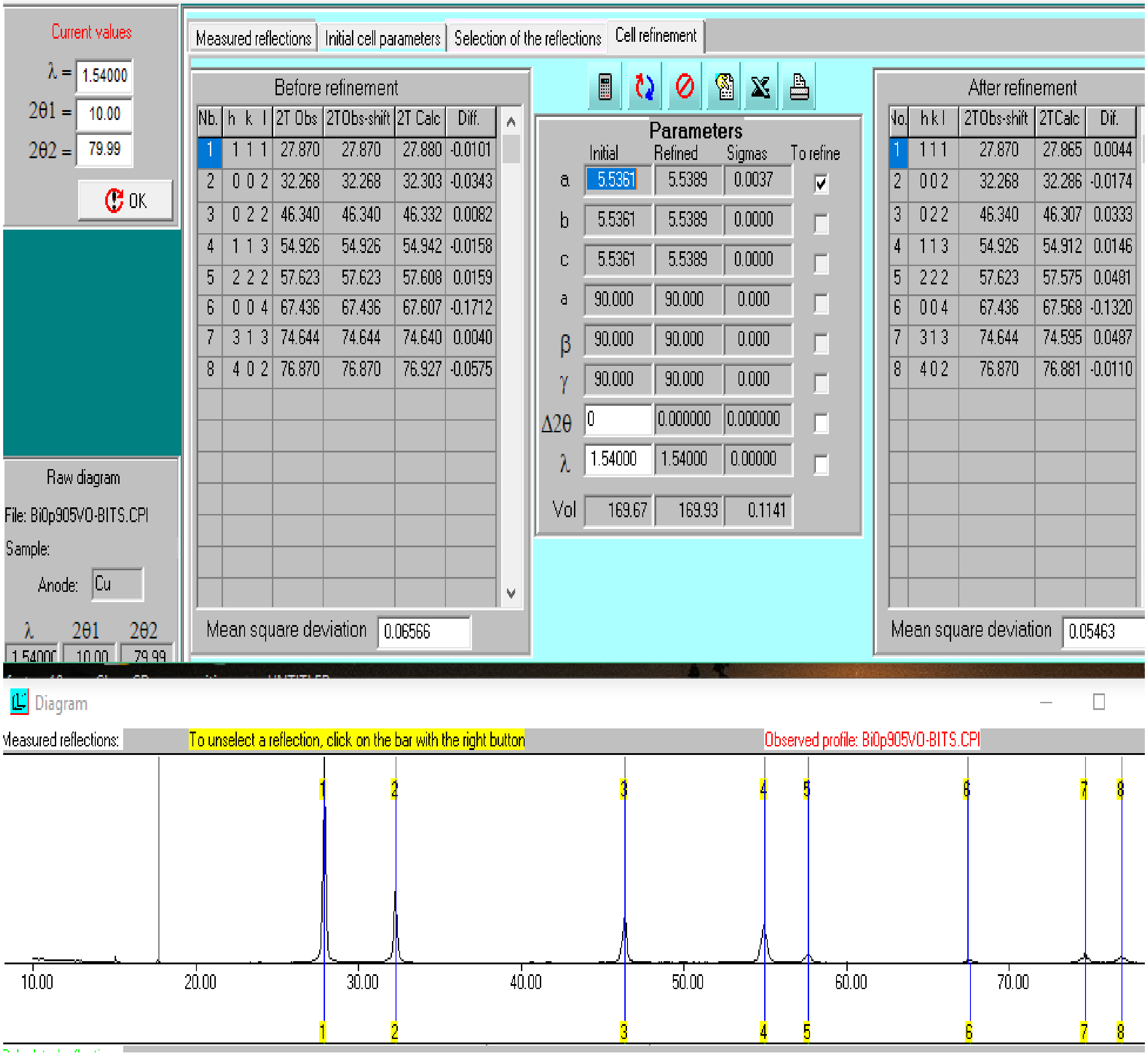

Current values

λ = 1.54000

2θ1 = 10.00

2θ2 = 79.99

Raw diagram

File: Bi0p905VO-BITS.CPI

Sample:

Anode: Cu

λ	2θ1	2θ2
1.5400	10.00	79.99

Before refinement

Nb.	h k l	2T Obs	2TObs-shift	2T Calc	Diff.
1	1 1 1	27.870	27.870	27.880	-0.0101
2	0 0 2	32.268	32.268	32.303	-0.0343
3	0 2 2	46.340	46.340	46.332	0.0082
4	1 1 3	54.926	54.926	54.942	-0.0158
5	2 2 2	57.623	57.623	57.608	0.0159
6	0 0 4	67.436	67.436	67.607	-0.1712
7	3 1 3	74.644	74.644	74.640	0.0040
8	4 0 2	76.870	76.870	76.927	-0.0575

Mean square deviation 0.06566

Parameters

	Initial	Refined	Sigmas	To refine
a	5.5361	5.5389	0.0037	☑
b	5.5361	5.5389	0.0000	☐
c	5.5361	5.5389	0.0000	☐
a	90.000	90.000	0.000	☐
β	90.000	90.000	0.000	☐
γ	90.000	90.000	0.000	☐
Δ2θ	0	0.000000	0.000000	☐
λ	1.54000	1.54000	0.00000	☐
Vol	169.67	169.93	0.1141	

After refinement

No.	h k l	2TObs-shift	2TCalc	Dif.
1	1 1 1	27.870	27.865	0.0044
2	0 0 2	32.268	32.286	-0.0174
3	0 2 2	46.340	46.307	0.0333
4	1 1 3	54.926	54.912	0.0146
5	2 2 2	57.623	57.575	0.0481
6	0 0 4	67.436	67.568	-0.1320
7	3 1 3	74.644	74.595	0.0487
8	4 0 2	76.870	76.881	-0.0110

Mean square deviation 0.05463

Measured reflections: To unselect a reflection, click on the bar with the right button

Observed profile: Bi0p905VO-BITS.CPI

Fig.17: XRD data analysis by CELREF for $Bi_{0.905}V_{0.095}O_{1.595}$

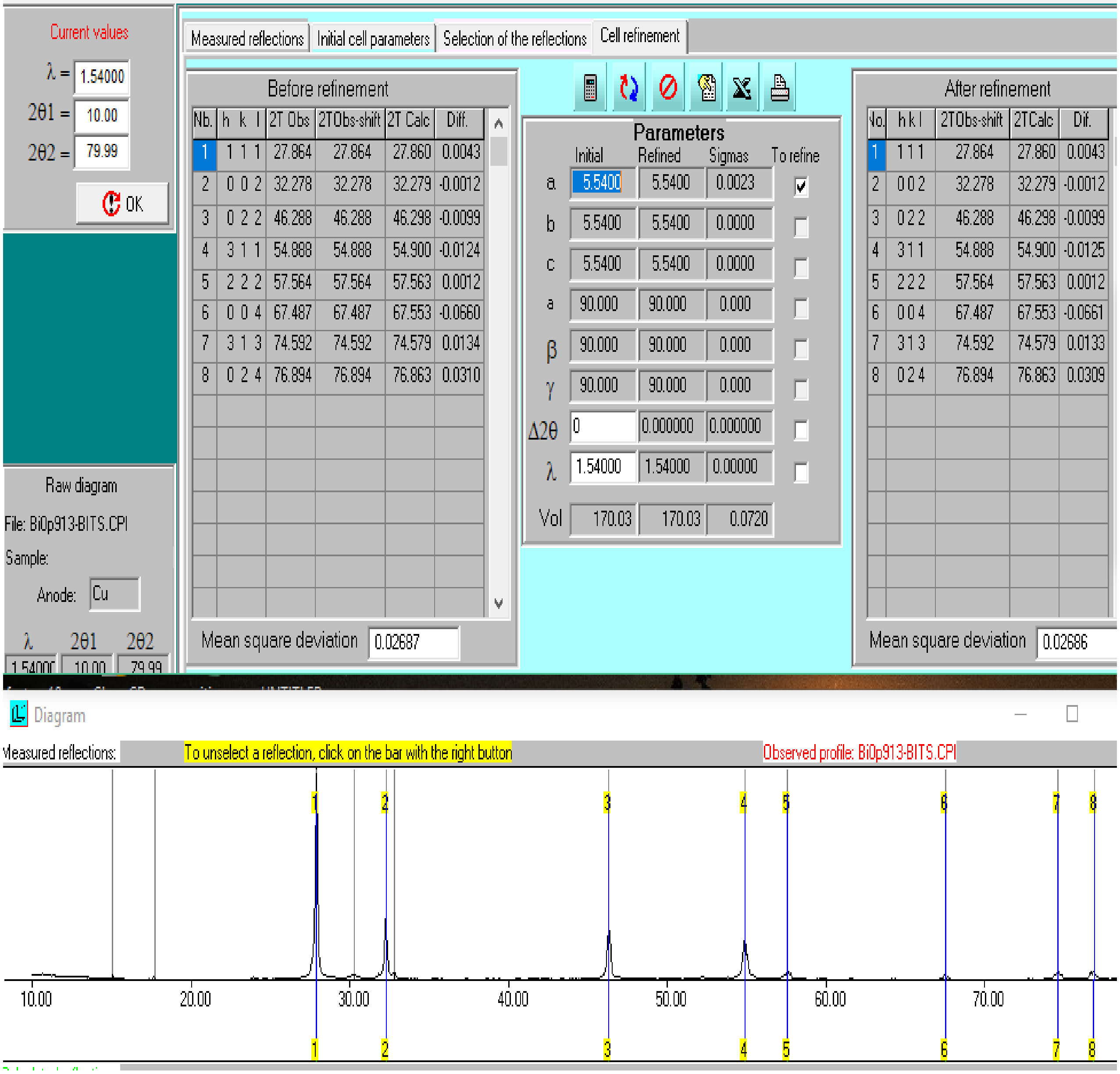

Current values

λ = 1.54000
2θ1 = 10.00
2θ2 = 79.99

Raw diagram

File: Bi0p913-BITS.CPI

Sample:

Anode: Cu

λ	2θ1	2θ2
1.5400	10.00	79.99

Before refinement

Nb.	h k l	2T Obs	2TObs-shift	2T Calc	Diff.
1	1 1 1	27.864	27.864	27.860	0.0043
2	0 0 2	32.278	32.278	32.279	-0.0012
3	0 2 2	46.288	46.288	46.298	-0.0099
4	3 1 1	54.888	54.888	54.900	-0.0124
5	2 2 2	57.564	57.564	57.563	0.0012
6	0 0 4	67.487	67.487	67.553	-0.0660
7	3 1 3	74.592	74.592	74.579	0.0134
8	0 2 4	76.894	76.894	76.863	0.0310

Mean square deviation 0.02687

Parameters

	Initial	Refined	Sigmas	To refine
a	5.5400	5.5400	0.0023	☑
b	5.5400	5.5400	0.0000	☐
c	5.5400	5.5400	0.0000	☐
a	90.000	90.000	0.000	☐
β	90.000	90.000	0.000	☐
γ	90.000	90.000	0.000	☐
Δ2θ	0	0.000000	0.000000	☐
λ	1.54000	1.54000	0.00000	☐
Vol	170.03	170.03	0.0720	

After refinement

No.	h k l	2TObs-shift	2TCalc	Dif.
1	1 1 1	27.864	27.860	0.0043
2	0 0 2	32.278	32.279	-0.0012
3	0 2 2	46.288	46.298	-0.0099
4	3 1 1	54.888	54.900	-0.0125
5	2 2 2	57.564	57.563	0.0012
6	0 0 4	67.487	67.553	-0.0661
7	3 1 3	74.592	74.579	0.0133
8	0 2 4	76.894	76.863	0.0309

Mean square deviation 0.02686

Fig.18: XRD data analysis by CELREF for $Bi_{0.913}V_{0.087}O_{1.587}$

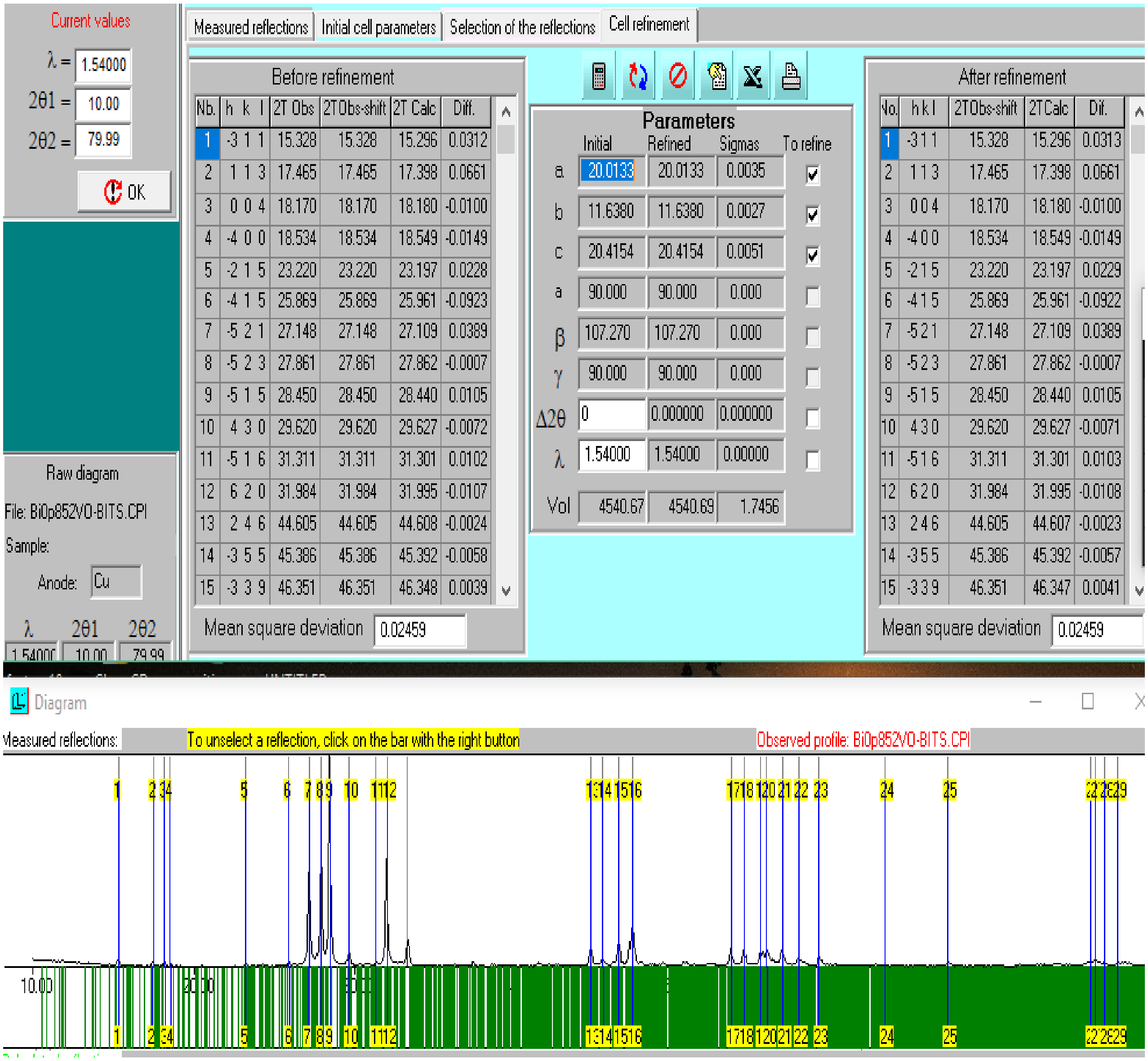

Current values

λ = 1.54000
2θ1 = 10.00
2θ2 = 79.99

Raw diagram
File: Bi0p852V0-BITS.CPI
Sample:
Anode: Cu

λ	2θ1	2θ2
1.54000	10.00	79.99

Before refinement

Nb.	h k l	2T Obs	2TObs-shift	2T Calc	Diff.
1	-3 1 1	15.328	15.328	15.296	0.0312
2	1 1 3	17.465	17.465	17.398	0.0661
3	0 0 4	18.170	18.170	18.180	-0.0100
4	-4 0 0	18.534	18.534	18.549	-0.0149
5	-2 1 5	23.220	23.220	23.197	0.0228
6	-4 1 5	25.869	25.869	25.961	-0.0923
7	-5 2 1	27.148	27.148	27.109	0.0389
8	-5 2 3	27.861	27.861	27.862	-0.0007
9	-5 1 5	28.450	28.450	28.440	0.0105
10	4 3 0	29.620	29.620	29.627	-0.0072
11	-5 1 6	31.311	31.311	31.301	0.0102
12	6 2 0	31.984	31.984	31.995	-0.0107
13	2 4 6	44.605	44.605	44.608	-0.0024
14	-3 5 5	45.386	45.386	45.392	-0.0058
15	-3 3 9	46.351	46.351	46.348	0.0039

Mean square deviation 0.02459

Parameters

	Initial	Refined	Sigmas	To refine
a	20.0133	20.0133	0.0035	☑
b	11.6380	11.6380	0.0027	☑
c	20.4154	20.4154	0.0051	☑
α	90.000	90.000	0.000	☐
β	107.270	107.270	0.000	☐
γ	90.000	90.000	0.000	☐
Δ2θ	0	0.000000	0.000000	☐
λ	1.54000	1.54000	0.00000	☐
Vol	4540.67	4540.69	1.7456	

After refinement

No.	h k l	2TObs-shift	2TCalc	Dif.
1	-3 1 1	15.328	15.296	0.0313
2	1 1 3	17.465	17.398	0.0661
3	0 0 4	18.170	18.180	-0.0100
4	-4 0 0	18.534	18.549	-0.0149
5	-2 1 5	23.220	23.197	0.0229
6	-4 1 5	25.869	25.961	-0.0922
7	-5 2 1	27.148	27.109	0.0389
8	-5 2 3	27.861	27.862	-0.0007
9	-5 1 5	28.450	28.440	0.0105
10	4 3 0	29.620	29.627	-0.0071
11	-5 1 6	31.311	31.301	0.0103
12	6 2 0	31.984	31.995	-0.0108
13	2 4 6	44.605	44.607	-0.0023
14	-3 5 5	45.386	45.392	-0.0057
15	-3 3 9	46.351	46.347	0.0041

Mean square deviation 0.02459

Measured reflections: To unselect a reflection, click on the bar with the right button

Observed profile: Bi0p852V0-BITS.CPI

Fig.19: XRD data analysis by CELREF for $Bi_{0.852}V_{0.148}O_{1.648}$

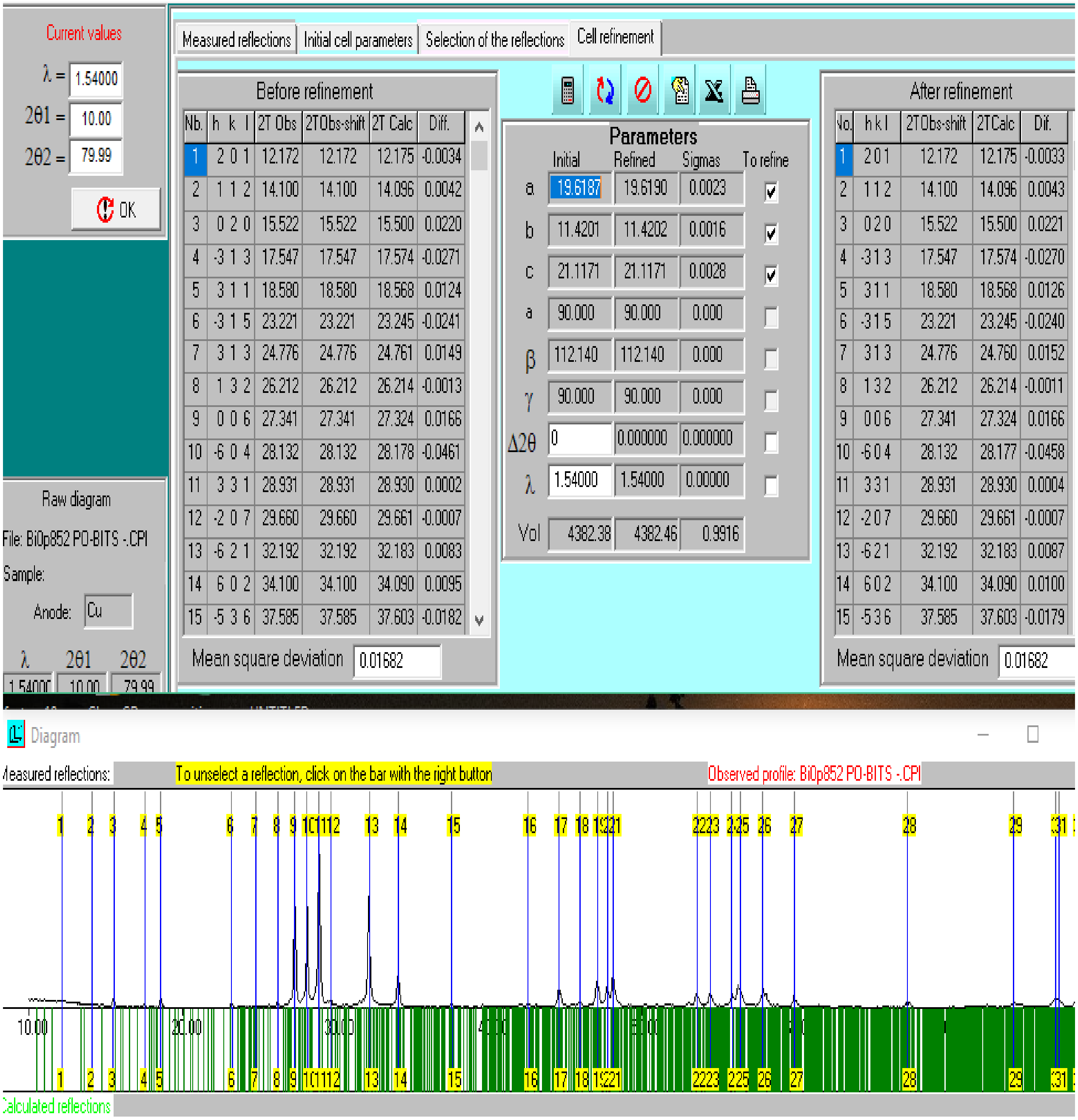

λ = 1.54000

$2\theta 1$ = 10.00

$2\theta 2$ = 79.99

File: Bi0p852 PO-BITS -.CPI

Sample:

Anode: Cu

λ	$2\theta 1$	$2\theta 2$
1.54000	10.00	79.99

Before refinement

Nb.	h k l	2T Obs	2TObs-shift	2T Calc	Diff.
1	2 0 1	12.172	12.172	12.175	-0.0034
2	1 1 2	14.100	14.100	14.096	0.0042
3	0 2 0	15.522	15.522	15.500	0.0220
4	-3 1 3	17.547	17.547	17.574	-0.0271
5	3 1 1	18.580	18.580	18.568	0.0124
6	-3 1 5	23.221	23.221	23.245	-0.0241
7	3 1 3	24.776	24.776	24.761	0.0149
8	1 3 2	26.212	26.212	26.214	-0.0013
9	0 0 6	27.341	27.341	27.324	0.0166
10	-6 0 4	28.132	28.132	28.178	-0.0461
11	3 3 1	28.931	28.931	28.930	0.0002
12	-2 0 7	29.660	29.660	29.661	-0.0007
13	-6 2 1	32.192	32.192	32.183	0.0083
14	6 0 2	34.100	34.100	34.090	0.0095
15	-5 3 6	37.585	37.585	37.603	-0.0182

Mean square deviation 0.01682

Parameters

	Initial	Refined	Sigmas	To refine
a	19.6187	19.6190	0.0023	☑
b	11.4201	11.4202	0.0016	☑
c	21.1171	21.1171	0.0028	☑
a	90.000	90.000	0.000	☐
β	112.140	112.140	0.000	☐
γ	90.000	90.000	0.000	☐
Δ2θ	0	0.000000	0.000000	☐
λ	1.54000	1.54000	0.00000	☐
Vol	4382.38	4382.46	0.9916	

After refinement

No.	h k l	2TObs-shift	2TCalc	Dif.
1	2 0 1	12.172	12.175	-0.0033
2	1 1 2	14.100	14.096	0.0043
3	0 2 0	15.522	15.500	0.0221
4	-3 1 3	17.547	17.574	-0.0270
5	3 1 1	18.580	18.568	0.0126
6	-3 1 5	23.221	23.245	-0.0240
7	3 1 3	24.776	24.760	0.0152
8	1 3 2	26.212	26.214	-0.0011
9	0 0 6	27.341	27.324	0.0166
10	-6 0 4	28.132	28.177	-0.0458
11	3 3 1	28.931	28.930	0.0004
12	-2 0 7	29.660	29.661	-0.0007
13	-6 2 1	32.192	32.183	0.0087
14	6 0 2	34.100	34.090	0.0100
15	-5 3 6	37.585	37.603	-0.0179

Mean square deviation 0.01682

Fig.20: XRD data analysis by CELREF for $Bi_{0.852}P_{0.148}O_{1.648}$

By comparing an observed Bragg's position with the calculated positions, one can also confirm the formation of expected structure of sample. Thus it was verified that $Bi_{0.905}V_{0.095}O_{1.595}$and $Bi_{0.913}V_{0.087}O_{1.587}$ has a cubic structure with space group symmetry Fm-3m, whereas $Bi_{0.852}V_{0.148}O_{1.648}$ and $Bi_{0.852}P_{0.148}O_{1.648}$ have monoclinic structure with space group P21/C and C2/m, respectively. The refined cell parameters of the samples are as tabulated below. Our results reveal that at lower V doping levels cubic phase is stabilized. Moreover, any other impurity phases have not been detected.

Table.5: Samples and refined cell parameters [36]

Samples	**Phase**	**Cell parameters**	**Space group**	**Unit cell Volume Å³**
$Bi_{0.905}V_{0.095}O_{1.595}$	Cubic	a=b=c=5.5389Å α=β=γ=90°	Fm-3m	169.93
$Bi_{0.913}V_{0.087}O_{1.587}$	Cubic	a=b=c=5.5400 Å α=β=γ=90°	Fm-3m	170.03
$Bi_{0.852}V_{0.148}O_{1.648}$	Monoclinic	a=20.0133 Å b=11.6380 Å c=20.4154 Å α= γ=90°, β=107.270 °	P21/C	4755.04
$Bi_{0.852}P_{0.148}O_{1.648}$	Monoclinic	a=19.6190 Å b=11.4202 Å, c=21.1171 Å α= γ=90°,β=112.140°	C2/m	4731.35

3.2 Energy band gap determination using Uv-Vis Spectroscopy

The optical properties of the prepared samples were analyzed by UV-Visible absorption technique. To determine the direct optical band gap, Tauc method was used with following equation

$$(\alpha h\nu)^2 = A(h\nu - E_g)$$

Where *h* is Planck's constant, ν is the frequency of the incident photon and A is a constant which depends on the electron-hole mobility. The optical band gap was determined via extrapolation of the plot of $(\alpha h\nu)^2$ vs. hν, where α=0 is set.

Tauc plots of $Bi_{1-x}V_xO_{1.5+x}$ (x=0.087, 0.095, 0.148) and $Bi_{0.852}P_{0.148}O_{1.648}$ are shown in below

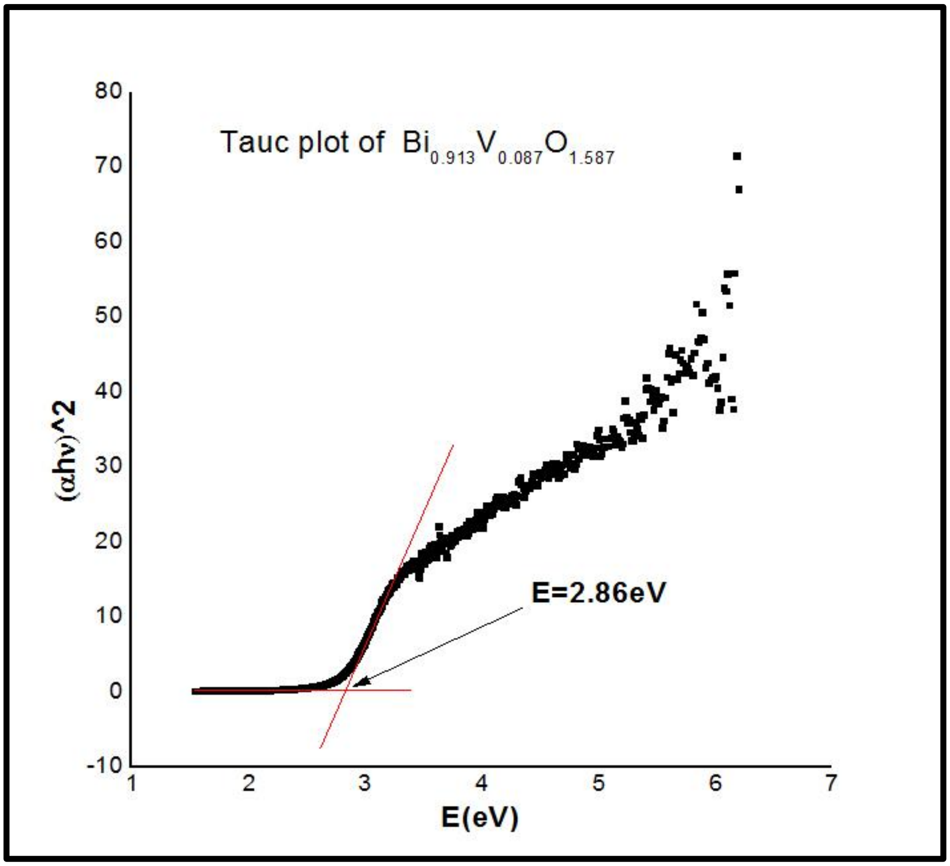

Fig.21: Tauc plot of $Bi_{0.913}V_{0.087}O_{1.587}$

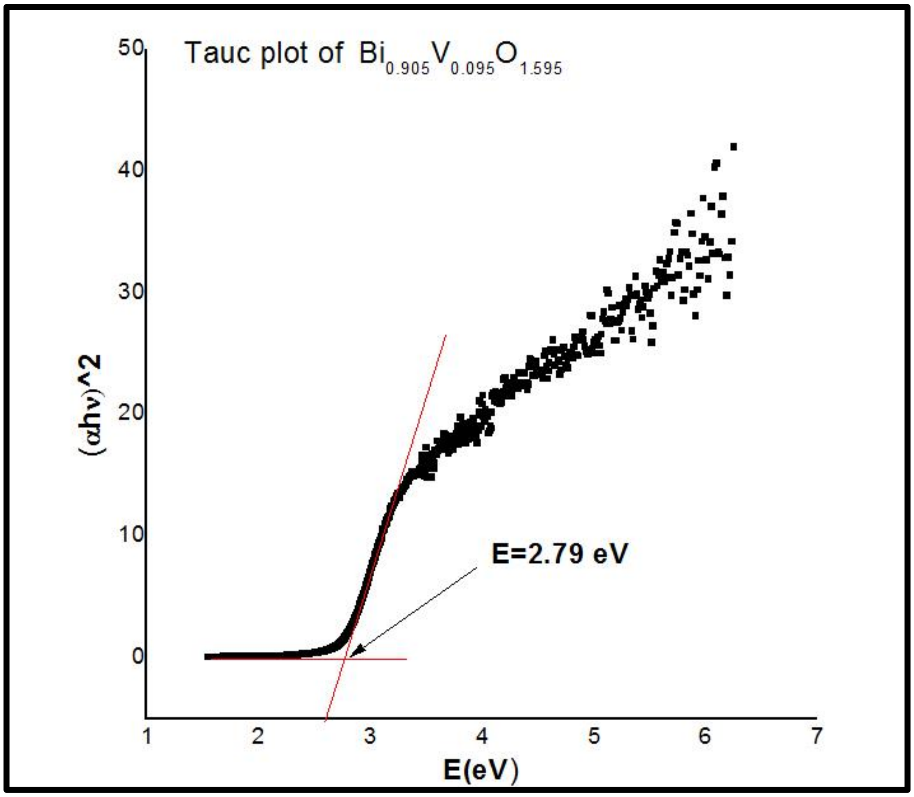

Fig.22: Tauc plot of $Bi_{0.905}V_{0.095}O_{1.595}$

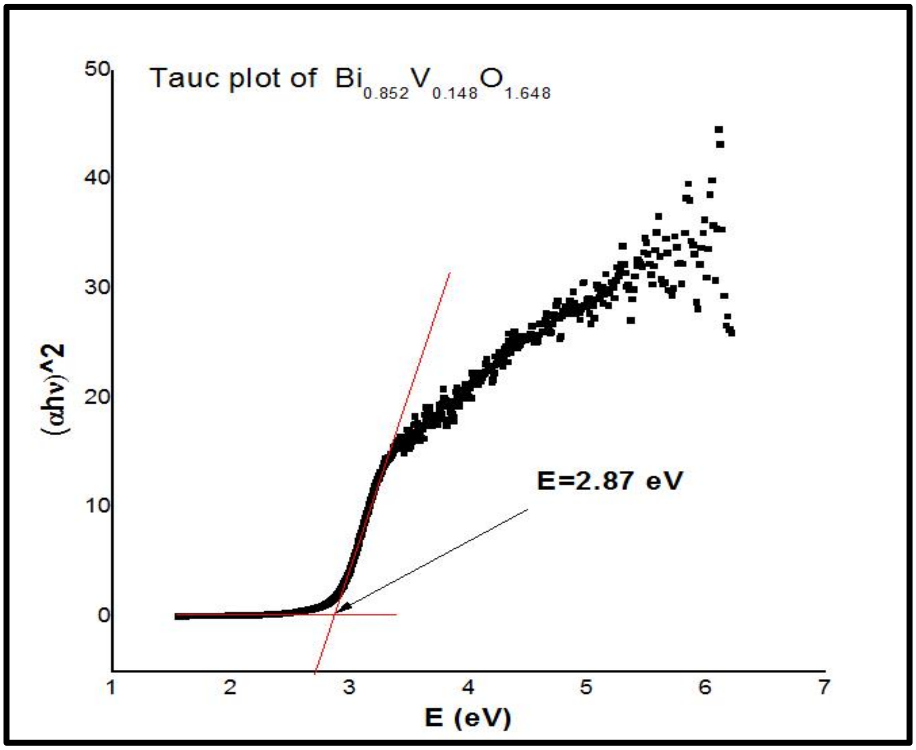

Fig.23: Tauc plot of $Bi_{0.852}V_{0.148}O_{1.648}$

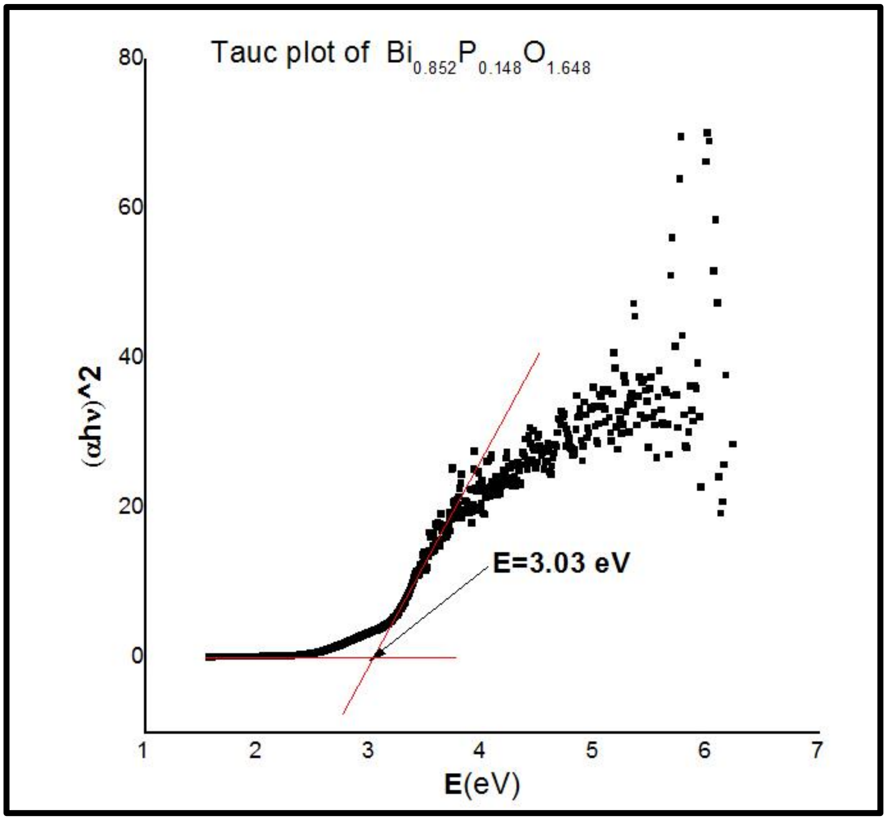

Fig.24: Tauc plot of $Bi_{0.852}P_{0.148}O_{1.648}$

The band gap value as determined from the Tauc plots are presented in table 1:

Table 6: Optical band gap values of prepared samples

Sample	**Energy band gap (eV)**
$Bi_{0.913}V_{0.087}O_{1.587}$	2.86
$Bi_{0.905}V_{0.095}O_{1.595}$	2.79
$Bi_{0.852}V_{0.148}O_{1.648}$	2.87
$Bi_{0.852}P_{0.148}O_{1.648}$	3.03

The values of band gap of $Bi_{1-x}V_xO_{1.5+x}$ with concentration x=0.087, 0.095, 0.148 and $Bi_{0.852}P_{0.148}O_{1.648}$ ranged from 2.79-3.03 eV, which indicates a good visible light absorption. Earlier literature reported that the δ-Bi_2O_3 has an optical band gap of around 2.4eV in accordance to Fan *et al.* On doping with Vanadium, this value was found to increase to 2.79-2.87eV. Also with rise in V concentration there was slight increase of band gap value. Phosphorus substitution also increased the band gap value. The energy band gap values determined in this study are higher than that of a semiconductor, where gap value is ~1 eV. Therefore, it is reasonable to consider that the electronic conductivity will be negligible. The negligible electronic conduction property of these materials meets the requirements of SOFC electrolytes.

3.3 Conductivity measurements using impedance spectroscopy

Impedance spectroscopy technique was used to determine the conductivity of the sample. Before impedance measurement, cylindrical pellets of the sample were coated with commercial silver paste on top and bottom surfaces. This was done to provide electrical contact. Impedance data was recorded in the temperature range of 50-400ºC and in the frequency range of 1 Hz-10 MHz.

Impedance data of $Bi_{1-x}V_xO_{1.5+x}$ (x=0.087, 0.095, 0.148) and $Bi_{0.852}P_{0.148}O_{1.648}$ samples are displayed in the form of Nyquist plots [Fig. 21-24].

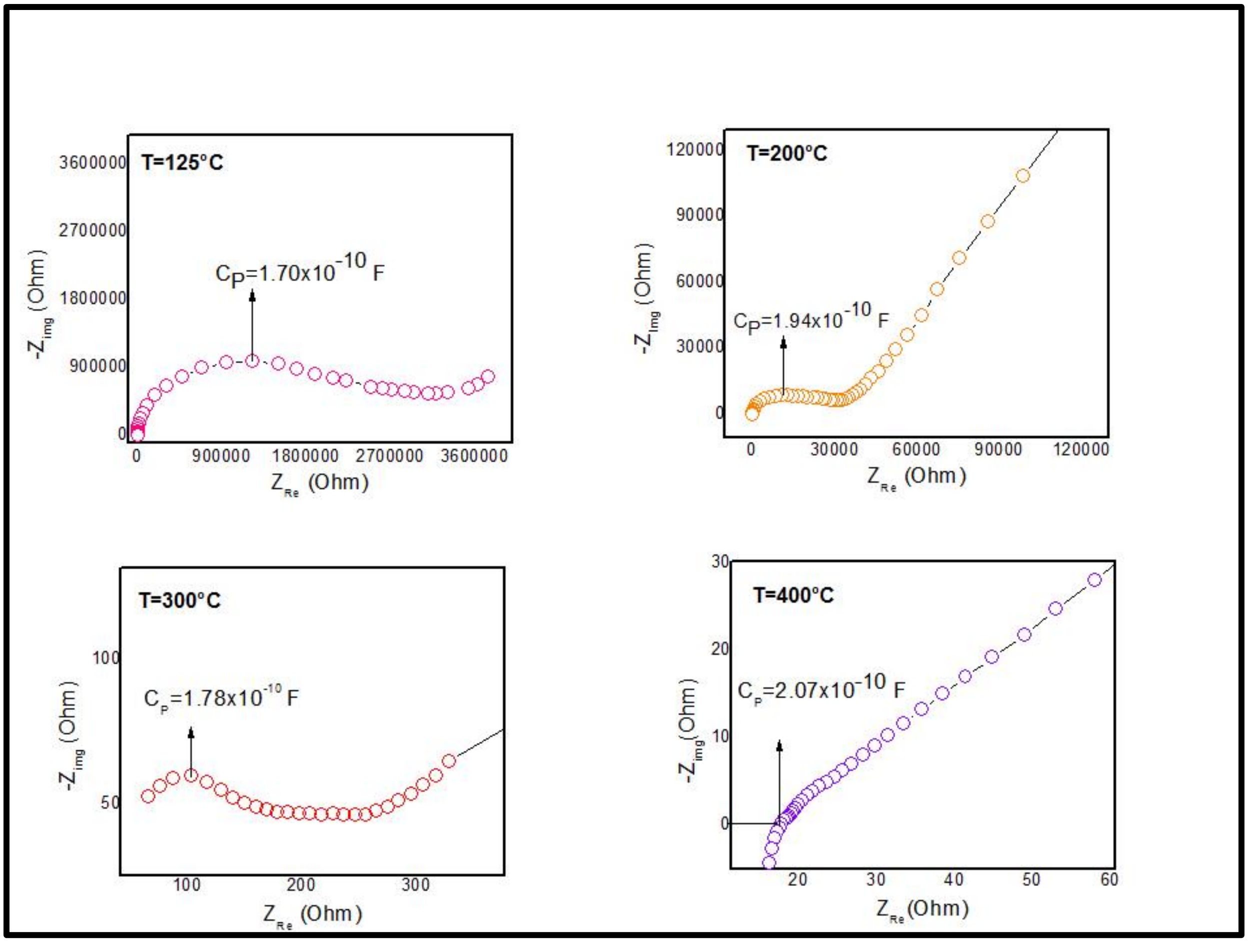

Figure 25: Complex impedance plane plot for $Bi_{0.913}V_{0.087}O_{1.587}$ at 4 different temperatures

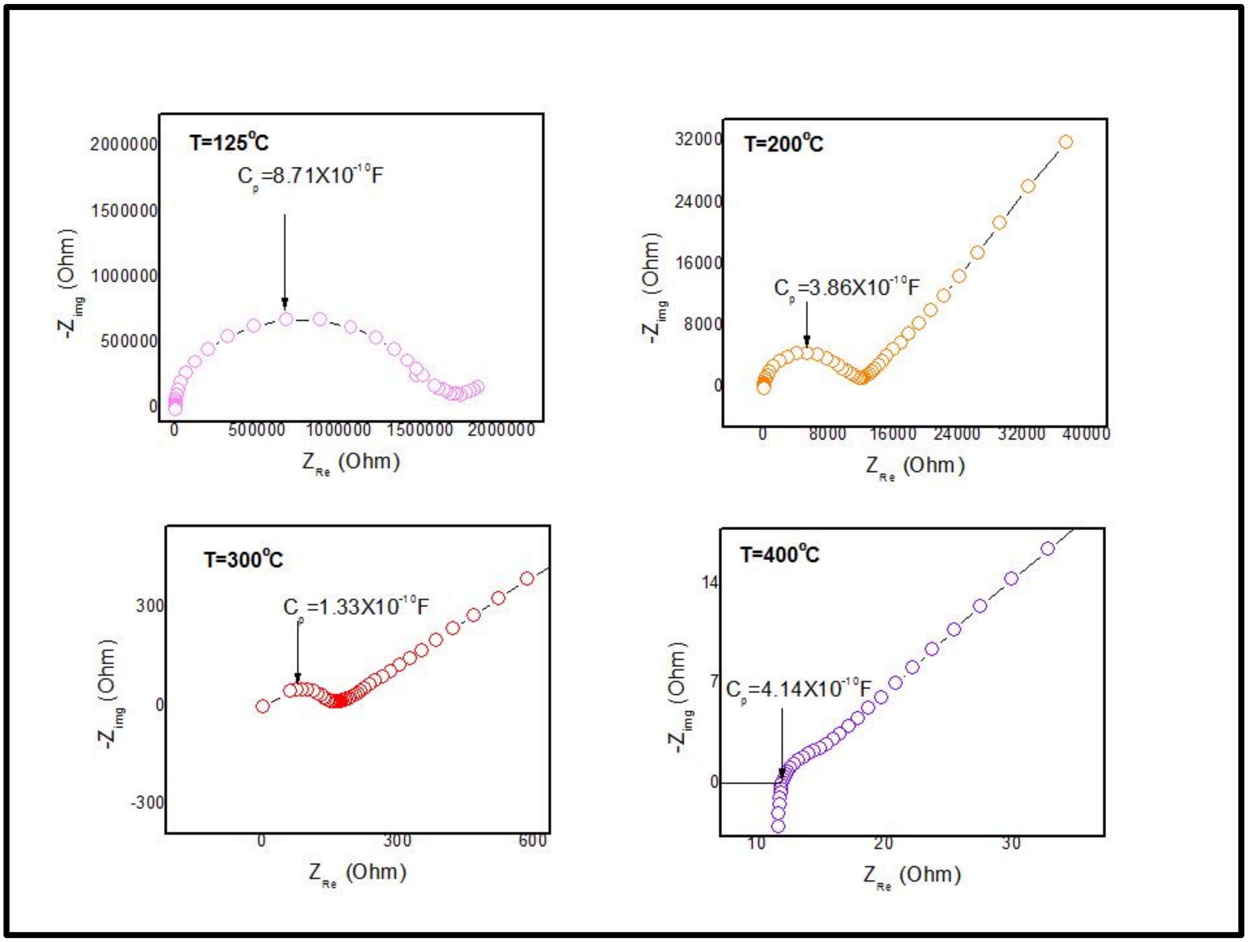

Figure 26: Complex impedance plane plot for $Bi_{0.905}V_{0.095}O_{1.595}$ at different temperatures

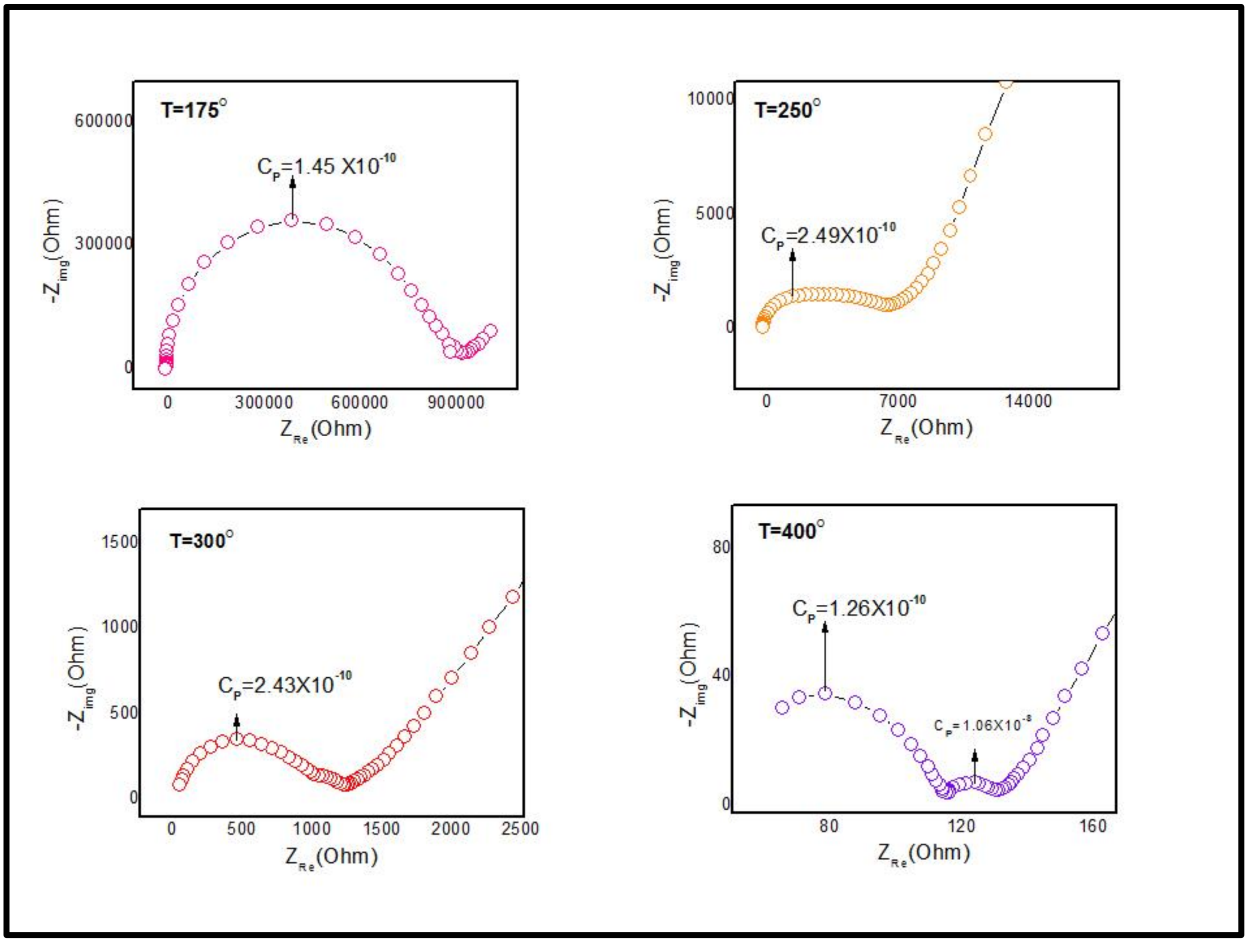

Figure 27: Complex impedance plane plot for $Bi_{0.852}V_{0.148}O_{1.648}$at different temperatures

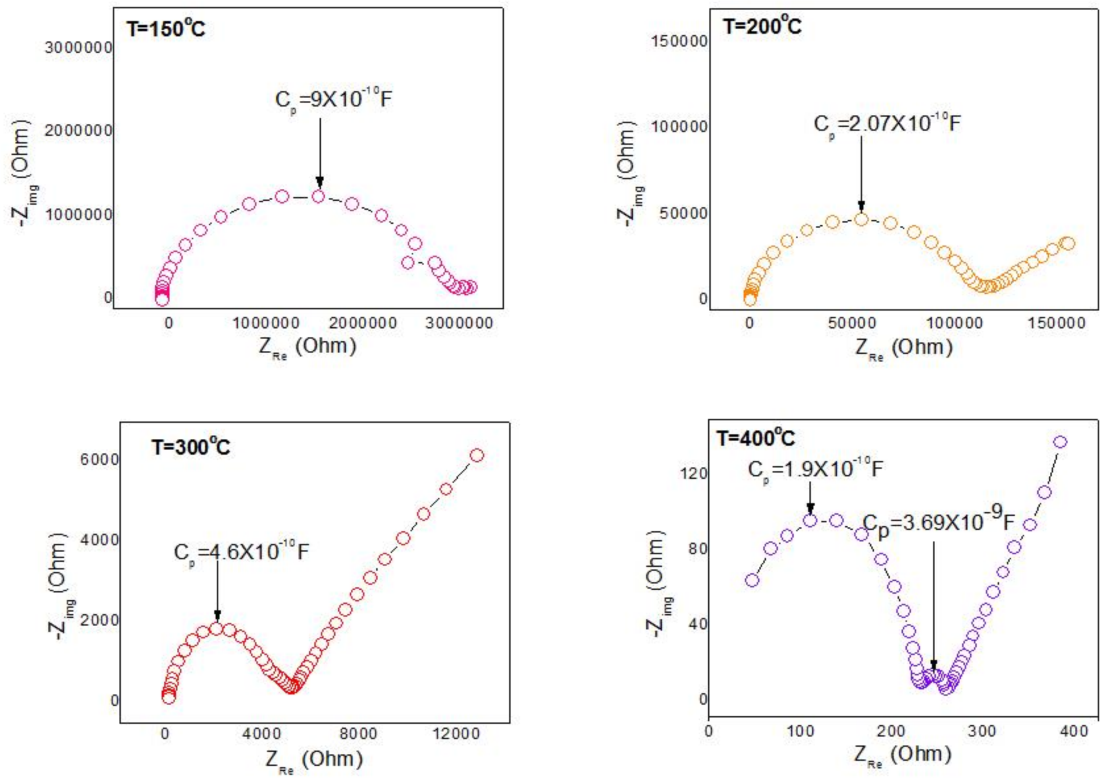

Figure 28: Complex impedance plane plot for $Bi_{0.852}P_{0.148}O_{1.648}$ at different temperatures

At low temperatures, the Nyquist plots show a broadened semicircle with a low-frequency spike due to the superimposition of bulk and grain boundary component and electrode-electrolyte interface resistances in the materials. Separate semicircle was not observed in some cases, this may possibly be due to very low grain capacitance. When temperature was increased; the semicircle became smaller and shifted towards lower Z values, indicating a reduction of grain and grain boundary resistance.

The broadened semicircle observed at low temperature could be resolved into two semicircles as shown in Figures. The capacitance of the high frequency semicircle has the value of the order ~10^{-10} F which is typical of the bulk component whereas the capacitance of the low frequency semicircle with value ~10^{-9} F is typical of grain boundary component. At higher temperatures, the predominant feature is a low-frequency spike inclined at the horizontal axis. It is a characteristic of ionic polarization phenomena occurring at the blocking electrodes, and thus supporting the idea that the conduction was predominantly ionic.

In order to determine conductivity for each composition of sample, we find the value of resistance R from the complex plane plots and substitute in equation given below

$$\sigma = \frac{1}{R}\frac{l}{A}$$

Where *R* is resistance, *l* is thickness of pellet and *A* is the area of the sample

The data of the total conductivity were used to plot the Arrhenius plot. Figure 25 shows the Arrhenius plot of conductivities for $Bi_{0.913}V_{0.087}O_{1.587}$, $Bi_{0.905}V_{0.095}O_{1.595}$, $Bi_{0.852}V_{0.148}O_{1.648}$ and $Bi_{0.852}P_{0.148}O_{1.648}$.

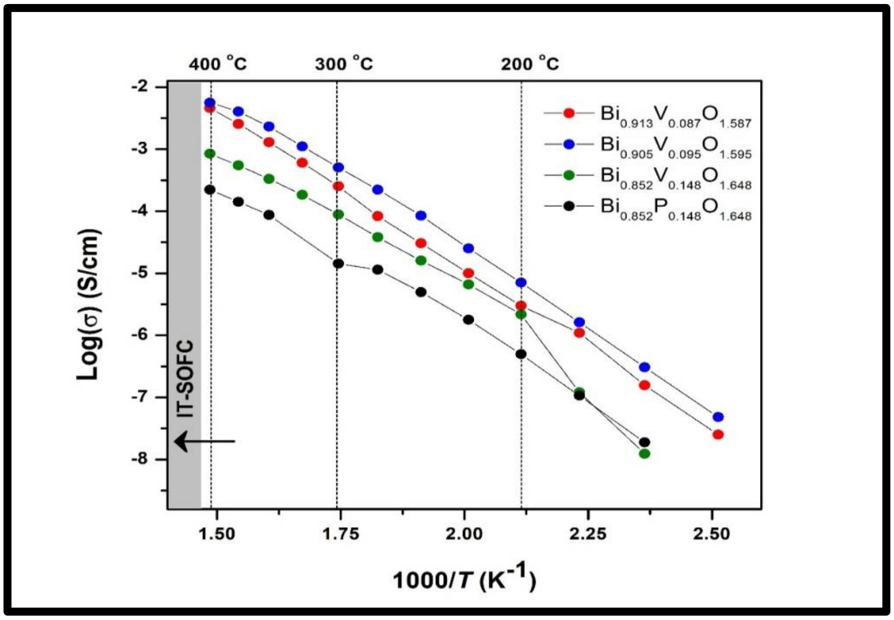

Fig.29: Arrhenius plot of conductivities for $Bi_{0.913}V_{0.087}O_{1.587}$, $Bi_{0.905}V_{0.095}O_{1.595}$, $Bi_{0.852}V_{0.148}O_{1.648}$ and $Bi_{0.852}P_{0.148}O_{1.648}$.

The total conductivity for all 4 samples at 400^0C is tabulated below

Table.7: Conductivity value of samples at T=400^0C

Sample	Conductivity at 400℃ (S/cm)
$Bi_{0.913}V_{0.087}O_{1.587}$	4.6×10^{-3}
$Bi_{0.905}V_{0.095}O_{1.595}$	5.6×10^{-3}
$Bi_{0.852}V_{0.148}O_{1.648}$	8.4×10^{-4}

$Bi_{0.852}P_{0.148}O_{1.648}$	2.2×10^{-4}

As can be seen in the Arrhenius plot, trend of conductivity for V doped samples $Bi_{1-x}V_xO_{1.5+x}$ where, x=0.087, 0.095, 0.148 at $T=400^0C$ is as expressed below

$$Bi_{0.905}V_{0.095}O_{1.595} > Bi_{0.913}V_{0.087}O_{1.587} > Bi_{0.852}V_{0.148}O_{1.648}$$

The ionic conductivity increases with dopant concentration due to an increase in oxide ion concentration, there exists an optimal dopant concentration corresponding to maximum ionic conductivity at a particular temperature. Above this optimal concentration the conductivity falls. This is because at higher dopant concentration, oxygen ion vacancies tend to associate with the dopants leading to a decrease of the concentration of free vacancies, and hence the conductivity. Also the substitution of Phosphorus for Vanadium decreases the conductivity as can be seen in the Arrhenius plot for the sample, $Bi_{0.852}P_{0.148}O_{1.648}$.Present investigation shows that the ionic conductivity of $Bi_{0.905}V_{0.095}O_{1.595}$ and $Bi_{0.913}V_{0.087}O_{1.587}$ compounds at 400 °C compares favourably to other popular electrolytes such as YSZ, LSGM, LAMOX, and Si/Ge-apatite.

CHAPTER 4

Conclusions & Future Scope

Conclusions:

- On V doping, samples exhibit highly conducting cubic phase, which however converts to monoclinic phase for higher V doping.
- High ionic conductivity for $0.087 < x < 0.095$ can be attributed to the increase in O^{2-}ion concentration. However, simultaneously it is important that some oxygen-vacancies are present in the structure to allow the hopping of O^{2-}ions to its adjacent vacant site. This may the reason why a higher V/P substitution does not allow a further increase of conductivity.
- The energy band gap of V substituted samples increases with increase in the concentration of V from x=0.087-0.148. This range of energy band gap values indicates negligible electronic conduction in the samples.

Future Scope:

- V, P-doping level can be carefully optimized to obtain maximum ionic conductivity.
- The ratio of oxygen vacancy and occupancy should be determined to find out the optimum condition for ion transports.
- Detailed structural studies are needed to understand the role of local and global structure on the ionic conduction property

References:

1) M. Lo. Faro *et al.*, “Intermediate temperature solid oxide fuel cell electrolytes”, *Journal of the Indian Institute of Science,* **89:4** (2009) 363.

2) A. M. Azad *et al.*, “Bismuth oxide- based solid electrolytes for fuel cells”, *Journal of material science.***29** (1994) 4135-4151.

3) Yamada *et al*., 2002

4) Wang Hay Kan *et al.*, “Trends in electrode development for next generation solid oxide fuel cells”, *J. Mater. Chem. A*, **4** (2016) 17913–17932.

5) L. Malavasi *et al.*, “Oxide-ion and proton conducting electrolyte materials for clean energy applications: structural and mechanistic features”, *Chem. Soc. Rev.*, **39,** (2010) ,4370

6) F. M. L. Figueiredo *et al.*“Electrolytes for solid oxide fuel cells”, *WIREs Energy Environ2012. doi: 10.1002/wene.23*

7) Tatsumi Ishihara, “Materials for High-temperature Fuel cells” Wiley (2013).

8) A. Hooper, “Fast ionic conductors”, *Contemporary Physics*, **19:2,** (1978) 147-168

9) Stephen J. Skinner *et al.*, “Oxygen ion conductors”, *Materials today*,**6** (2003) 30-37

10) Joseph R. Peet *et al*., “Insight into Design of improved Oxide Ion Conductors: Dynamics and Conduction Mechanisms in $Bi_{0.913}V_{0.087}O_{1.587}$ solid electrolytes”, *J. Am. Chem. Soc.,***141**, (2019) 9989-9997

11) West A. R., “*Solid State Chemistry and its Applications”* John Wiley & Sons, Ltd (2014).

12) P. Shuk *et al.*, “Oxide ion conducting solid electrolytes based on Bi_2O_3”, *Solid State Ionics*, **89** (1996) 179–196.

13) A. Laarif *et al.*, “The lone pair concept and the conductivity of bismuth Oxides Bi_2O_3”*Solid State Ionics*, **21** (1986) 183.

14) P.D Battle *et al.*, “Structural and dynamical studies of δ-Bi_2O_3 oxide ion conductors”, *Journal of Solid State Chemistry*,**63**(1986) 8-15.

15) https://www.google.com/search?q=solid+phase+of+bi2O3&source=lnms&tbm=isch&sa=X&ved=2ahUKEwiA0anq49znAhUA7HMBHb03CcwQ_AUoAXoECA0QAw&biw=1422&bih=978#imgrc=aPQN7Rm8WgMnpM

16) https://www.google.com/search?q=http://www.chegg.comhomework.help/questions.and.answers/zirconium-dioxide-zro2-adopts-fluorite-crystal-shown-lattice-parameter-517&rlz=1C1CHBD_enIN819IN819&source=lnms&tbm=isch&sa=X&ved=2ahUKEwjwiprd5NznAhUa6nMBHQxCAoYQ_AUoAXoECAMQAw&biw=1422&bih=978#imgrc=tuk7DpTn7hj2GM

17) https://www.google.com/search?q=http%3A%2F%2Fwww.ikts.fraunhofer.de%2Fen%2Fdepartments%2Fenergy+bio-medical+technology%2Fmaterials+and+components%2Fsofc+stack.+development.html&tbm=isch&ved=2ahUKEwi21M2Y5tznAhXDSisKHZ42DesQ2-cCegQIABAA&oq=http%3A%2F%2Fwww.ikts.fraunhofer.de%2Fen%2Fdepartments%2Fenergy+bio-medical+technology%2Fmaterials+and+components%2Fsofc+stack.+development.html&gs_l=img.3...94787.97013..97887...0.0..4.248.875.0j4j1......0....1..gws-wiz-img.....0.bFcfWOg7zUo&ei=ObxMXvbTGsOVrQGe7bTYDg&bih=979&biw=1403&rlz=1C1CHBD_enIN819IN819&hl=en#imgrc=BwIFD75-74pS-M

18) L. J. Gauckler *et al., “*Solid Oxide Fuel Cells: Systems and Materials*”, Chimia,***58** (2004) 837-850

19) S.C. Singhal *, “Advances in solid oxide fuel cell technology”, Solid State Ionics,***135,** Issue 1-4 (2000)305-313

20) https://www.doitpoms.ac.uk/tlplib/fuel-cells/sofc_electrode_materials.php

21) https://en.wikipedia.org/wiki/Bismuth(III)_oxide

22) Andrei A. Bunaciua *et al., “X-Ray Diffraction: Instrumentation and Applications”, Critical Reviews in Analytical Chemistry,* 45:4 (2015) 289-299

23) West A. R., “*Solid State Chemistry and its Applications”* John Wiley & Sons, Ltd (2014), 239-241

24) Zhebo Chen and Thomas F. Jaramillo (n.d). *The Use of UV-visible Spectroscopy to Measure the Band Gap of a Semiconductor,* Department of Chemical Engineering, Stanford University Edited by Bruce Brunschwig 09/19/2017

25) Clark, B. J., Frost, T., & Russell, M. A. (1993*). UV Spectroscopy: Techniques, instrumentation and data handling.* London; New York: Chapman & Hall

26) Instrumentation and characterization Technique-Anna university, Chennai-shodhganga

27) Pankove, J. I., “*Optical process in semiconductors*”, Prentice-Hall Inc., Englewood Cliffs, New Jersey, 1971, Ch-11.

28) Sze, S.M. & Kwok K. Ng., “*Physics of Semiconductor devices*” Wiley eastern Ltd., New Delhi (1979) p.52

29) https://en.wikipedia.org/wiki/Band_gap

30) https://eng.libretexts.org/Bookshelves/Materials_Science/Supplemental_Modules_(Materials_Science)/Insulators/Electrochemical_Impedance_Spectroscopy

31) J. T. S. Irvine et al., “*Electroceramics: Characterization by Impedance Spectroscopy”, Adv. Mater.* **2** (1990) 132-134

32) Armstrong, R.D. and M. Todd. 1995. Interfacial electrochemistry. *In Solid State Electrochemistry*, ed. P.G. Bruce. Great Britain: Cambridge University Press.

33) Cogger, N. D., Evans, N. J. *An Introduction to Electrochemical Impedance Measurement*, 1999 Technical Note,Solartron Analytical Technical Report No. 6, Part No. BTR006, http://www.solartronanalytical.com/downloads/technotes/technote06.pdf

34) Reece, C., 2005. An Introduction to Electrochemical Impedance Spectroscopy (EIS). https://www.jlab.org/conferences/tfsrf/Thursday/Th_2_1-EISintroReece.pdf. Accessed March 27 2020

35) Mario F. García-Sánchez *et al., “*An Elementary Picture of Dielectric Spectroscopy in Solids: Physical Basis*”,Journal of Chemical Education*, **80** (2003) 1062.

36) Matthew T. Dunstan *et al.*, “Variable-Temperature Multinuclear Solid-State NMR Study of Oxide Ion Dynamics in Fluorite-Type Bismuth Vanadate and Phosphate Solid Electrolytes”,*Chem. Mater.*.**31** (2019) 1704-1714.